Design and Analysis of Innovative Circular Polarized High Gain Feed-Reflector and Phased Array Antenna System Solutions

Ghanshyam Mishra and Satish K. Sharma

July 2, 2020

Publication Number: CSRCR2020-04

Computational Science & Engineering Faculty and Students Research Articles

Database Powered by the Computational Science Research Center Computing Group & Visualization Lab

COMPUTATIONAL SCIENCE & ENGINEERING

SAN DIEGO STATE UNIVERSITY

Computational Science Research Center
College of Sciences
5500 Campanile Drive
San Diego, CA 92182-1245
(619) 594-3430

SDSU-UCI COMPUTATIONAL SCIENCE JDP

RESEARCH EXAMINATION REPORT

Design and Analysis of Innovative Circular Polarized High Gain Feed-Reflector and Phased Array Antenna System Solutions

---

JDP student:

Ghanshyam Mishra

Thesis advisor:

Prof. Satish K. Sharma

Research Examination Report

December 6th 2018

Abstract

The report presents a novel W-band left-hand circular polarized (LHCP) cylindrical waveguide feed horn antenna. The proposed antenna features an inbuilt polarizer structure and a single side-fed linear polarized input to offer symmetric LHCP radiation pattern. The internal polarizer structure consists of 9 pairs of circular cavities to generate a circularly polarized wave, eliminating the need for an orthomode transducer or a complex septum. The side-fed horn reduces the overall length by eliminating rectangular to circular waveguide transition. The proposed horn antenna's electrical dimension is $7.2\lambda \times 3.9\lambda \times 1.4\lambda$ at 84 GHz. The antenna has impedance matching (S_{11} below -15 dB) and axial ratio below 1.2 dB from 79.5 GHz to 88 GHz. The horn is used as a feed source for an offset parabolic reflector of 10 cm diameter and small *f*/*D* ratio 0.25 which can fit inside a CubeSat. The feed reflector assembly is also simulated with the complete aluminum CubeSat chassis to obtain effective RHCP gain of 35 dBic. The measurement of the prototyped feed horn and the offset parabolic reflector antenna validates the analysis and simulation results.

List of Publications, Patent disclosure and Research Award direct from this research

Journal Paper:

G. Mishra, S. K. Sharma, J. S. Chieh "A Circular Polarized Feed Horn with Inbuilt Polarizer for Offset Reflector Antenna for W-band CubeSat Applications," *IEEE Transaction on Antennas and Prop.*, [Accepted for publication].

Patent Disclosure:

S. K. Sharma, J. S. Chieh, **G. Mishra**, and A. Castro, "Circular Polarized Waveguide Feedhorn with Internal Polarizer Structure," [US Patent Disclosure approved].

Conference Papers:

1. **G. Mishra**, S. K. Sharma and J. S. Chieh, "Analysis and Design of a W-Band Circular Polarized Feed Horn with Inbuilt Polarizer for Low f/D Offset Reflector Antenna," *URSI EM Theory Symposium, EMTS* 2019, [Submitted as Young Scientist Award (YSA) paper].
2. **G. Mishra**, A. T. Castro, S. K. Sharma and J. S. Chieh, "W-band feed horn with polarizer structure for an offset reflector antenna for cubesat applications," *2017 IEEE International Symposium on Antennas and Propagation & USNC/URSI National Radio Science Meeting*, San Diego, CA, USA, 2017, pp. 557-558.

Research Award:

Director's Award for outstanding poster and oral presentation entitled "W-band feed horn with polarizer structure for an offset reflector antenna for CubeSat applications, *ACSESS 2017*, San Diego.

Table of Contents

1 Objective

In this research, we proposed the development of a CubeSat beacon which will allow for high data rate downlinks of at least 200 Mbps for remote sensing applications in the W-Band. The analysis and design of a W-band (79 GHz to 88 GHz) left hand circular polarization (LHCP) feed horn with stable radiation pattern performance is developed and is integrated with an offset parabolic reflector antenna of $f/D = 0.25$ to achieve a minimum right hand circular polarization (RHCP) gain of 34 dBic to maintain the data link.

2 Motivation

CubeSats have evolved from an educational platform allowing universities to develop cost effective flight-ready spacecraft to standard platforms which allow for advanced technology demonstrations. Most CubeSats are used for earth science observation including optical, infrared, and microwave imaging for things such as atmospheric properties including clouds and precipitation, land topography and soil moisture, ocean surface salinity and temperature, snow and ice cover, and gravity and magnetic field monitoring. CubeSats occupy the low earth orbit (LEO) at 500 km above the earth, with the ceiling at 2180 km. All of these remote sensing applications generate large amounts of data, which require a SATCOM downlink with high data rates. Although wideband SATCOM links do exist currently, spectrum demand is only increasing. Many researchers have proposed using the millimeter-wave frequency band for SATCOM because it is relatively uncrowded and allows for high fractional bandwidths.

The W-band frequency spectrum is advantageous because of its wide swath of available bandwidth which is uncrowded, and more importantly, there is an O_2 absorption window between 80 to 100 GHz, which allows for low atmospheric attenuation, as shown in Fig. 2.1.

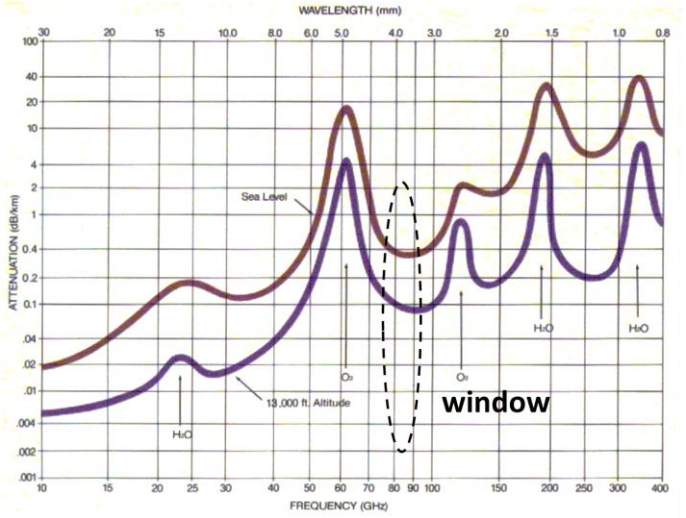

Fig. 2.1. Atmospheric attenuation vs. frequency

3 Introduction

Circular polarized electromagnetic waves are preferred for space to ground satellite communications (SATCOM), owing to its resilience to scintillation and other scattering effects. Reflector antennas with circularly polarized (CP) feed sources provide high gain solutions for satellite communication systems [1], [2]. CubeSats are miniaturized satellites that typically reside in the low earth orbit (LEO) with configurations ranging from 1U – 6U sizes (1U represents a 10 cm x 10 cm x 10 cm cube). High gain CP antenna systems are necessary to maintain the reliable communication link. A CP wave is realized by combining two orthogonal linear polarized (LP) signals with 90° time-phase difference. In [3], a dual CP feed polarizer is designed using an array of metallic pins as delay structure to achieve the desired phase shift for the generation of circular polarization. The losses of the pins along with the fabrication challenge limit the use of this method at millimeter-wave frequencies. In [4], a LP-CP conversion is achieved at sub-mm -wave frequencies by exploiting differential dispersion in hexagonal waveguides. This design overcomes the need for waveguide partitions and assemblies often required for CP horns, and it is potentially less susceptible to fabrication tolerances owing to hollow waveguide structure.

In an orthomode transducer (OMT), the CP wave is generated by combining the two orthogonal linear polarized signals in the compact waveguide structure [5]-[14]. This approach requires a dual input source with hybrid or septum that increases the complexity, especially at millimeter-wave frequencies due to smaller feature sizes. In the septum polarizer based method, the CP wave is generated from a single linear polarized signal [15]-[18]. The septum is a stepped ridge structure in the middle of the rectangular waveguide. The length and number of stepped ridges affect the axial ratio and the polarization quality. The benefit of this method is that the structure is compact, offers wideband CP and a single input is necessary. However, the septum is an asymmetric structure which leads to difficulty in the fabrication and degradation of radiation performances at millimeter-wave [1], [19].

In [20], the metallic ridges are embodied inside the rectangular waveguide to induce CP from a linear polarized wave. This method is similar to the septum method in [15] and [16]. The orthogonal signals are created from a tapered ridge waveguide; however, the construction requires the ridge waveguide to be stepped in size and thus piecewise fabrication is needed, adding complexity. Dielectric loaded circular horn antenna and substrate integrated waveguides based OMT generated CP approaches are discussed in [21]-[28]. The dielectric loaded waveguides offer compact design but suffer from high dielectric losses at millimeter-wave frequencies along with the fabrication challenges.

CubeSat at microwave and millimeter-wave frequencies demand compact and high gain antenna solutions. In [29]-[32], a 0.5 m deployable mesh reflector antenna with $f/D = 0.5$ is developed for high gain and wide matching bandwidth at Ka-band. The deployable mechanism becomes necessary due to the lower frequency of operation at Ka-band. It requires a stowage volume of 1.5U and a complex deployment mechanism with stubs and 30 folding ribs. An alternate high gain deployable antenna solution for CubeSat is provided with the reflectarray antenna at X-band [33]. It has narrow matching bandwidth (< 5 %) and deployed size of 33.5 cm × 59.7 cm. In [34], a 118 GHz radiometer antenna is designed for a 3U CubeSat. The radiometer payload module is compact

and embedded inside the CubeSat chassis. However, the antenna is linear polarized and has *f*/*D* ratio of 0.56.

In this research, a W-band left-hand circular polarized (LHCP) feed horn antenna with an inbuilt polarizer structure with single input is proposed. The proposed polarizer portion is electrically longer than the conventional polarizers, but it incorporates good performance with easy fabrication process. This feed horn antenna provides impedance matching (S_{11}) below -15 dB and axial ratio (AR) below 1.2 dB from 79.5 GHz to 88 GHz, in addition to the symmetric radiation pattern. The initial simulation results for the feed horn antenna are presented in [35]. This feed horn antenna is integrated with an offset parabolic reflector of *f*/*D* = 0.25 for CubeSat application. The proposed feed reflector antenna can fit inside the 1U volume of the CubeSat owing to the high frequency of operation at W–band, without a complex deployable mechanism. The prototype of the feed horn and offset reflector antenna is fabricated and the measured results are in excellent agreement with the simulation. The measured right-hand circular polarized (RHCP) gain of the reflector antenna is above 34 dBic and the total measured efficiency is above 60% within the desired bandwidth.

This report is organized as follows. Section 4 characterizes the propagating channel at W-band and presents the link budget. Section 6 discusses the need for a compact *f*/*D* = 0.25 offset reflector and the corresponding feed requirements for this configuration. The proposed feed antenna geometry and its principle of operation with the parametric studies are presented in section 7. In addition, all the necessary modifications in the proposed feed horn design and its simulation results are shown. Integration of the proposed feed horn with the offset parabolic reflector and its simulation performances are shown in section 8. The experimental results for the proposed feed horn and the offset parabolic reflector antenna is presented in section 9. The effect of the CubeSat chassis on the radiation performance of the proposed feed reflector antenna is presented in section 10. Full wave simulation of the feed horn antenna is carried in Ansys HFSS. The offset reflector is analyzed using Ticra GRASP which utilizes Physical Optics (PO) currents on the reflector and Physical Theory of Diffraction (PTD) rim currents to obtain the total induced current on the reflector.

4 Link Budget Calculation

Although the prospect of high data rates is attractive at the millimeter-wave frequencies, the reality is that at these frequencies the wavelength is much smaller, and the associated free space path loss and propagation loss is much higher. Therefore, characterization of the propagating channel between 75 – 110 GHz is critical, and using a CubeSat to do this is ideal. The benefit of operation in this band is that given a limited volume, the gain of the antenna is much higher.

Fig. 4.1 shows some of the underlying assumptions that were used in the link budget calculations. We approximated the distance between the ground station and the CubeSat at zenith to be 500km. At 60˚ away, the distance increases to 1000km. Table 1 shows the link budget calculations for a LEO downlink using Ka-, Q-, and W-Bands. Calculations are for clear sky links, which do not include the effects of heavy clouds and rain. The Tx antenna size was constrained to 1U diameter of 10 cm and the propagation loss was calculated based on O_2 and H_2O absorption curves. Propagation loss in the millimeter-wave regime is often said to be severe, this is true, albeit only

for terrestrial radio links. For SATCOM applications, the effective atmosphere really extends only about 8 km, and so the propagation loss due to atmospheric absorption is actually fairly minimal. As can be seen, link margins from 4.92 to 10.92 dB can be attained for distances of 1000km and 500km respectively. In practice, a 10 dB link margin is probably realistic. From available literature, CubeSats typically occupy LEO usually in a circular orbit at an attitude of 500 km. As can be seen, a 200 Mbps link can be obtained in the W-Band at 86 GHz with a modest link margin of 10.92 dB at a distance of 500 km.

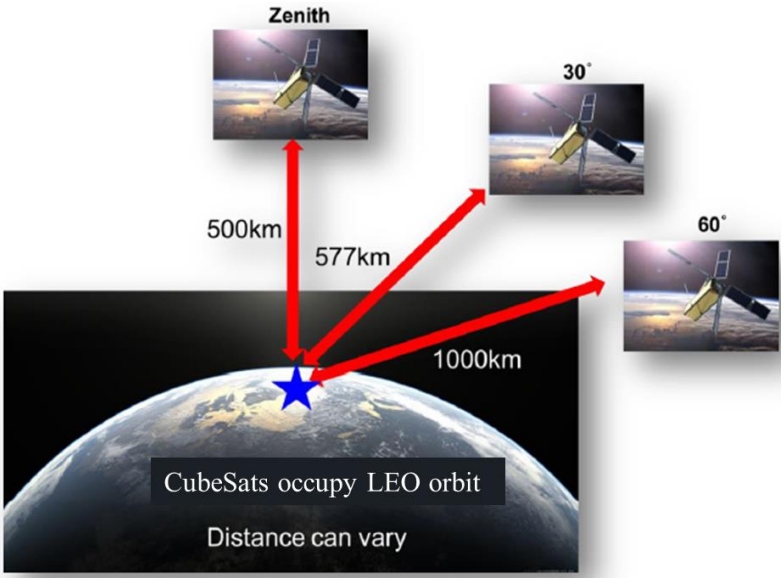

Fig. 4.1. Assumptions for link budget calculations.

	ka-Band (35 GHz)	Q-Band (55 GHz)	W-Band (86 GHz)	Unit
Satellite Transmitter Power	1	1	0.6	W
Satellite Transmitter Power	30	30	28	dBm
Tx Losses	-3	-3	-3	dB
Tx Implementation Loss (Phase Noise)	-2	-2	-2	dB
Tx Antenna Gain (10 cm dish)	30	33	35	dBic
Tx EIRP	**55**	**58**	**58**	**dBm**
Path Loss (2180 Km LEO)	-166	-194	-197	dB
Polarization Loss	-0.5	-0.5	-0.5	dB
Antenna Misalignment Loss	-1	-1	-1	dB
Other Misc. Losses (Atmosphere ITU Rec 676-9)	-1	-6	-3	dB
Isotropic Signal Level receive Station	-113.5	-143.50	-143.50	dBm
Rx Antenna Gain (2 m dish)	60	61	65	dBic
Rx Signal Level	**-53.5**	**-82.50**	**-78.50**	**dBm**
Rx Noise Temperature	170	438	627	K
Rx Noise Figure (Hittite)	2	4	5	dB
Channel Bandwidth	50	50	100	MHz
Rx Noise power	-99.31	-95.20	-93.64	dBm
Rx G/T	38	35	37	dB/K
Rx C/No	45.81	15.70	15.14	dBHz
Rx Eb/No (FEC 0.75, 8 PSK)	42.8	12.7	12.14	dB
Required Rx Eb/No (8 PSK BER 10E-6)	14	14	14	dB
Data Rate	**100**	**100**	**200**	**Mbps**
Link Margin (2180 km)	**28.8**	**-1.3**	**-1.86**	**dB**
Link Margin (1000 km)	**35.6**	**5.49**	**4.92**	**dB**
Link Margin (500 km)	**41.6**	**11.49**	**10.92**	**dB**

Table 1. Downlink budget for Ka-, Q-, and W-Bands for various distances

5 Review of Computational Methods used in the Research

5.1 Finite Element Method

Finite Element Method (FEM) is a computational tool for engineers and physicists, utilizing rapid computations to solve large problems insoluble by analytical, closed-form expressions. The "Finite Element Method" involves subdividing a large problem into individually simple constituent units which are each soluble via direct analytical methods, then reassembling the solution for the entire problem space as a matrix of simultaneous equations. FEM software can solve mechanical (stress, strain, vibration), aerodynamic or fluid flow, thermal, or electromagnetic problems. Ansys HFSS (High Frequency Structure Simulator) simulation tool is used to set up the FEM problem for the proposed feed horn antenna. A brief overview of the FEM method employed in HFSS is summarized in this section.

The model is subdivided into tetrahedral elements and basis function, W_n is defined per tetrahedral. W_n define conditions between nodal locations in the overall mesh of tetrahedra, based on the problem inputs. The functions are simple and nonzero only within the tetrahedra. These basis functions are then multiplied by field equation. Following are the steps in the HFSS FEM solution process.

HFSS solves field equation derived from Maxwell's equations

$$\nabla \times \left(\frac{1}{\mu_r} \nabla \times \vec{E} \right) - k_o^2 \varepsilon_r \vec{E} = 0 \tag{5.1.1}$$

Integrating the result over volume, we get

$$\int_V \left[W_n \cdot \nabla \times \left(\frac{1}{\mu_r} \nabla \times \vec{E} \right) - k_o^2 \varepsilon_r W_n \vec{E} \right] dV = 0 \tag{5.1.2}$$

Integration is replicated in thousands of equations for n =1, 2 ...N. Intent is to obtain N equations with N unknowns for solution.

The equation is rewritten, using Green's and Divergence theorems
Set equal to excitation/boundary terms:

$$\int_V \left[(\nabla \times W_n) \bullet \left(\frac{1}{\mu_r} \nabla \times \vec{E} \right) - k_o^2 \varepsilon_r W_n \vec{E} \right] dV = \int_S (boundary\, term) dS \tag{5.1.3}$$

The E-field is written as summation of unknowns, x_m, times same basis functions used in generating the initial series of equations

$$\vec{E} = \sum_{m=1}^{N} x_m W_m \tag{5.1.4}$$

Resulting equations allow solution of unknowns, x_m, to find E

$$\sum_{m=1}^{N} x_m \cdot \left(\int_V \left[(\nabla \times W_n) \bullet \left(\frac{1}{\mu_r} \nabla \times W_m \right) - k_o^2 \varepsilon_r W_n W_m \right] dV \right) = \int_S (boundary\ term) dS \tag{5.1.5}$$

Note: Equation has the basic form $Ax = B$, where

A is the basis functions and field equation, in a known $N \times N$ matrix

'x' is the unknowns to be solved for

B is the excitation

The Finite-Element solution matrix has a number of known characteristics such as:

- Size: Matrix is generally large, N on the order of tens of thousands.
- Density: Matrix is generally *sparse*, with a large number of zero entries.
- Only basis functions in the same tetrahedra result in nonzero entries.
- Banding: Intelligent ordering of the mesh results in nonzero entries being clustered along the diagonal.
- Lossless problems will have only *real* nonzero entries.
- Lossy problems will have *complex* nonzero entries.
- Problems with standard excitations ('ports') will have *symmetric* matrices.
- Problems with certain boundary conditions (e.g. 'linked') may have *asymmetric* matrices

Due to its sparse and banded nature, the matrix can be solved using mathematical matrix decomposition techniques. HFSS uses an iterative *Multifrontal Matrix Solver*. Matrix equations are thus formulated to solve for electromagnetic field behavior. The flowchart of the general design process in Ansys HFSS is illustrated in Fig. 5.1.1.

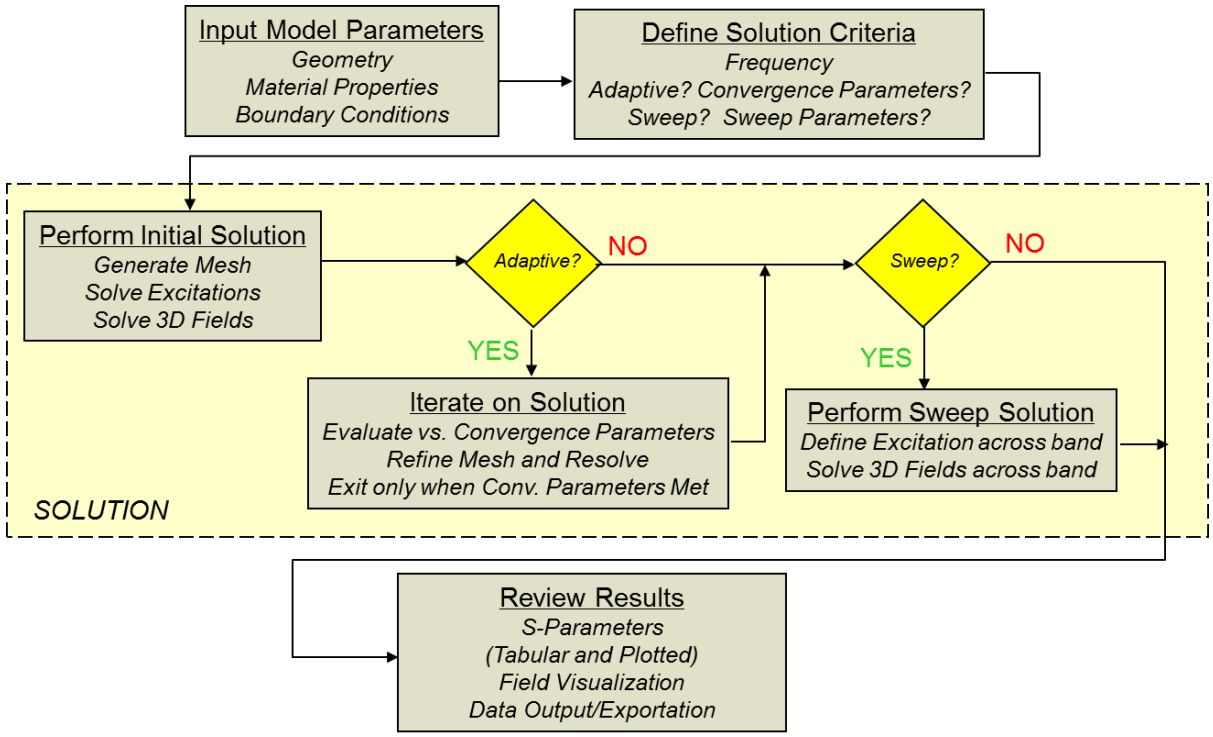

Fig. 5.1.1 Flowchart of the general design process in Ansys HFSS. [Online: https://www.ansys.com/products /electronics/ansys-hfss].

5.2 Asymptotic High Frequency Methods

Reflector analysis are based on asymptotic high-frequency expansions of Maxwell's equations. They are high frequency methods that are only accurate when the dimensions of the objects being analyzing are large compared to the wavelength of the field. The asymptotic techniques briefly introduced in the following sections include physical optics, geometrical optics, and shooting and bouncing rays.

5.2.1 Current Distribution Method: Physical optics (PO)

Physical optics (PO) assumes that the incident field from the feed is known, and that it excites surface currents ($\mathbf{J_s}$) on the reflector's surface as $\mathbf{J}_s = 2\hat{\mathbf{n}} \times \mathbf{H}^i$. Once the induced surface currents $\mathbf{J_s}$ are found on the reflector's surface, the magnetic vector potential **A** and the far-zone field can be calculated.

In practice, the electric far field is calculated directly from $\mathbf{J_S}$ by

$$\mathbf{E}^{far} = -j\omega\mu \frac{e^{-j\beta r}}{4\pi r} \iint_{S_r} \left[\mathbf{J}_s - \left(\mathbf{J}_s \bullet \hat{\mathbf{r}} \right) \hat{\mathbf{r}} \right] e^{j\beta \hat{r} \bullet r'} ds' \qquad (5.2.1.1)$$

This equation follows directly from the relation between the far-zone electric field and the magnetic vector potential **A**,

$$\mathbf{E}^{far} = -j\omega \mathbf{A}_{\perp} \qquad (5.2.1.2)$$

which can be written formally as

$$\mathbf{E}^{far} = -j\omega \mathbf{A} - \left(-j\omega \mathbf{A} \bullet \hat{\mathbf{r}} \right) \hat{\mathbf{r}} = -j\omega \left(A_\theta \hat{\theta} + A_\phi \hat{\phi} \right) \qquad (5.2.1.3)$$

This approach is also known as Rusch's method. Ticra Grasp is used to evaluate the PO based field patterns with respect to any aperture shape and any aperture current distribution.

5.2.2 Aperture Distribution Analysis via Geometric Optics (GO)

With the *aperture distribution method*, the electric field is first determined over a plane, which is normal to the reflector's axis, and it lies at the focal point (the *antenna aperture*). GO (ray tracing) is used to determine the electric field. Equivalent sources are formed over the aperture plane. It is assumed that the equivalent sources are zero outside the reflector's aperture. The radiation pattern is then computed from the electric field on the focal-plane aperture.

Ticra Grasp tool is used to perform the GO analysis of the reflector. The following provides the brief overview of the reflector radiation pattern when a feed with a rotationally symmetric pattern is placed at the focal point which has its axis inclined at an angle ψ relative to the axis of the reflector.

If the feed is made from coaxial circular waveguides excited by TE_{1m} and TM_{1m} modes, it will have radiation pattern of the form [*R. E. Collin, "Antennas and Radio wave propagation", McGraw-Hill Higher Education, Feb 1, 1985*].

$$\mathbf{E}_f = \frac{e^{-jk_0 r}}{r}\left[\mathbf{a}_{\theta_0} e_1(\theta_0)\sin(\phi_0) + \mathbf{a}_{\phi_0} e_2(\theta_0)\cos(\phi_0)\right] \qquad (5.2.2.1)$$

For a circular symmetric pattern with no cross polarization

$$e_1(\theta_0) = e_2(\theta_0) = e(\theta_0)$$

The reflected pattern at reflector surface is given by

$$\mathbf{E}_r = -\mathbf{E}_f + 2\left(\mathbf{n}\cdot\mathbf{E}_f\right)\mathbf{n} \qquad (5.2.2.2)$$

A considerable amount of algebra is involved to obtain the focal-plane aperture field. In the simplification procedure the following relations are used:

$$v = f - \frac{\rho^2}{4f}$$

$$r = 2f - v$$

$$4fr = 4f^2 + \rho^2$$

$$r + v\cos\psi + u\sin\psi = \frac{4f^2 + \rho^2 + 4fu\sin\psi + \left(4f^2 - \rho^2\right)\cos\psi}{4f}$$

The focal-plane aperture fields are as follows:

$$E_{ax} = \frac{4fe^{-j2k_0 f}e(\theta_0)}{\left(4f^2+\rho^2\right)\left[4f^2+\rho^2-4fy\sin\psi+\left(4f^2-\rho^2\right)\cos\psi\right]}\times\left[2xy(1-\cos\psi)-4fx\sin\psi\right] \qquad (5.2.2.3)$$

$$E_{ay} = \frac{4fe^{-j2k_0 f}e(\theta_0)\times\left[\left(4f^2+\rho^2-2x^2\right)+\left(4f^2-\rho^2+2x^2\right)\cos\psi-4fy\sin\psi\right]}{\left(4f^2+\rho^2\right)\left[4f^2+\rho^2-4fy\sin\psi+\left(4f^2-\rho^2\right)\cos\psi\right]} \qquad (5.2.2.4)$$

$$E_{az} = 0 \qquad (5.2.2.5)$$

where, $\rho^2 = x^2 + y^2$ and $\theta_0 = \cos^{-1}\left(\frac{4f^2-\rho^2}{4f^2+\rho^2}\cos\psi - \frac{4fy}{4f^2+\rho^2}\sin\psi\right)$

If the feed pattern polarized along *x* axis by rotating the feed by 90°, then the feed pattern is

$$\mathbf{E}_f = \frac{e^{-jk_0 r}}{r}e(\theta_0)\left(\mathbf{a}_{\theta_0}\cos(\phi_0) - \mathbf{a}_{\phi_0}\sin(\phi_0)\right) \qquad (5.2.2.6)$$

For this case, the focal-plane aperture field is found to be

$$E_{ax} = \frac{-4fe^{-j2k_0 f}e(\theta_0)\times\left[\left(4f^2+\rho^2-2x^2\right)+\left(4f^2-\rho^2+2x^2\right)\cos\psi-4fy\sin\psi\right]}{\left(4f^2+\rho^2\right)\left[4f^2+\rho^2-4fy\sin\psi+\left(4f^2-\rho^2\right)\cos\psi\right]} \tag{5.2.2.7}$$

$$E_{ay} = \frac{4fe^{-j2k_0 f}e(\theta_0)}{\left(4f^2+\rho^2\right)\left[4f^2+\rho^2-4fy\sin\psi+\left(4f^2-\rho^2\right)\cos\psi\right]}\times\left[2xy(1-\cos\psi)-4fx\sin\psi\right] \tag{5.2.2.8}$$

$$E_{az} = 0 \tag{5.2.2.9}$$

In general, the feed pattern for coaxial feeds does not have rotational symmetry. A non-symmetrical feed pattern may be expressed in the form

$$\mathbf{E}_f = \frac{e^{-jk_0 r}}{r}e_1(\theta_0)\left(\mathbf{a}_{\phi_0}\sin(\phi_0)+\mathbf{a}_{\phi_0}\cos(\phi_0)\right)+\frac{e^{-jk_0 r}}{r}\left[e_2(\theta_0)-e_1(\theta_0)\right]\left(\mathbf{a}_{\phi_0}\cos(\phi_0)\right)$$

The asymmetrical part contributes an additional aperture field given by

$$\begin{aligned} E_f^{'} &= \frac{4fe^{-j2k_0 f}\left[e_2(\theta_0)-e_1(\theta_0)\right]}{\left(4f^2+\rho^2\right)\left[4f^2+\rho^2-4fy\sin\psi+\left(4f^2-\rho^2\right)\cos\psi\right]} \\ &\times\frac{a_x[-4fxy\cos\psi-x(4f^2-\rho^2+2x^2)\sin\psi]+a_y[4fx^2\cos\psi-2x^2y\sin\psi]}{[4f^2+\rho^2+4fy\sin\psi-(4f^2-\rho^2)\cos\psi]/4f} \end{aligned} \tag{5.2.2.10}$$

The far-zone radiation field, computed from the aperture electric field, is given as

$$\mathbf{E} = \frac{jk_0}{2\pi r}e^{-jk_0 r}\left[\mathbf{a}_\theta\left(f_x\cos\phi+f_y\sin\phi\right)+\mathbf{a}_\phi\left(f_y\cos\phi-f_x\sin\phi\right)\cos\theta\right] \tag{5.2.2.11}$$

where the following Fourier transforms are used:

$$\begin{aligned} f_x(k_x,k_y) &= \int_{S_a}E_{ax}(x,y)e^{jk_x x+jk_y y}dxdy \\ f_y(k_x,k_y) &= \int_{S_a}E_{ay}(x,y)e^{jk_x x+jk_y y}dxdy \end{aligned} \tag{5.2.2.12}$$

and $k_x = k_0\sin\theta\cos\phi$, $k_x = k_0\sin\theta\sin\phi$

For a *y*-polarized aperture field, the co-polarized field is the component along the unit vector $a_1 = a_\theta\sin\phi+a_\phi\cos\phi$. Thus we find

$$E_{COPOL} = \frac{jk_0 e^{-jk_0 r}}{2\pi r}\left\{ f_y[1+(\cos\theta-1)\cos^2\phi] - f_x(\cos\theta-1)\frac{\sin 2\phi}{2}\right\} \qquad (5.2.2.13)$$

The cross-polarized field is the component along the unit vector $a_2 = a_\theta \cos\phi - a_\phi \sin\phi$ and is given by

$$E_{X-POL} = \frac{jk_0 e^{-jk_0 r}}{2\pi r}\left\{ f_x[1+(\cos\theta-1)\sin^2\phi] + f_y(1-\cos\theta)\frac{\sin 2\phi}{2}\right\} \qquad (5.2.2.14)$$

The cross-polarized field is generally high in the $\phi = \pm 45^\circ$ inter-cardinal planes but may also be high in the $\phi = 0^\circ$ and 90° planes if the cross-polarized aperture field is large.

We note that both the GO and the PO methods produce accurate results for the main beam and first sidelobe. The far off angle pattern from the main beam can be accurately predicted by including diffraction effects (scattering) from the reflector's rim. This is done by augmenting GO with the use of geometrical theory of diffraction (GTD), or by augmenting the PO method with the physical theory of diffraction (PTD).

An offset fed parabolic reflector antenna is analyzed in MATLAB using Ray optics method or Aperture distribution method. The feed source used is *y*-polarized dominant TE_{11} mode. The results are compared with the Ticra GRASP's physical optics (PO) based method. It can be observed that both the methods produce accurate results.

<u>The following data was used</u>

- Projected aperture diameter =1.2m
- Feed tilt angle = 26.6^0
- Focal length f = 48.77 cm
- Frequency =12 GHz

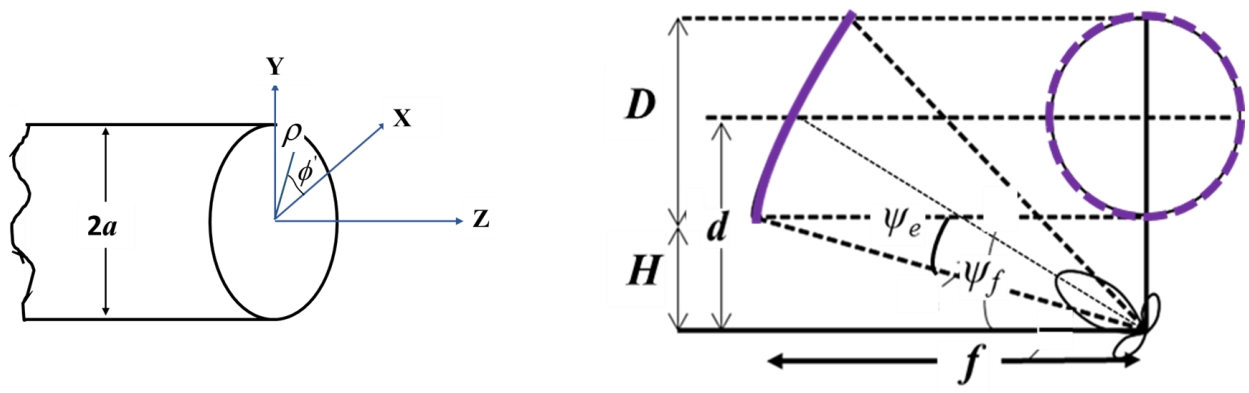

(a) (b)

Fig. 5.2.2.1 (a) open ended circular waveguide section as a feedhorn and (b) offset parabolic reflector in an orthographic projection.

The dominant mode in a circular waveguide as shown in Fig. 5.2.2.1(a) is *TE11* mode for which the electric field distribution over the cross section is [*R. E. Collin, "Antennas and Radio wave propagation", McGraw-Hill Higher Education, Feb 1, 1985*].

$$E_\rho = \frac{2\sin\phi}{\rho} J_1\left(1.84\frac{\rho}{a}\right)$$
$$E_\phi = \frac{2a\cos\phi}{1.84}\frac{dJ_1(1.84\rho/a)}{d\rho} \qquad (5.2.2.15)$$

where J_1 is the Bessel function of the first kind and order 1 and ρ is the cylindrical radial coordinate shown in Fig 5.2.2.1(a). In rectangular coordinate system, the expressions for the field distribution are given by

$$E_x = E_\rho\cos\phi - E_\phi\sin\phi$$
$$E_y = E_\rho\sin\phi + E_\phi\cos\phi \qquad (5.2.2.15)$$

If we assume aperture field is approximated by these expressions, then it is relatively easy to derive the corresponding radiated fields. The exponential factor involved in the far field radiated field is $e^{jk_x x' + jk_y y'}$, where

$$k_x x' + k_y y' = k_0\rho\sin\theta\left(\cos\phi\cos\phi' + \sin\phi\sin\phi'\right)$$

$$= k_0\rho\sin\theta\cos\left(\phi - \phi'\right)$$

Thus, the radiated far-field of the circular waveguide in *TE11* mode is given by

$$E_\theta = \frac{jk_0}{r}e^{-jk_0 r}2a^2\sin\phi\frac{J_1(1.84)}{1.84}\frac{J_1(u)}{u}$$
$$E_\phi = \frac{jk_0}{r}e^{-jk_0 r}2a^2\cos\phi\cos\theta\left[\frac{1.84J_1(1.84)}{1.84^2 - u^2}J_1'(u)\right] \qquad (5.2.2.16)$$

where $u = k_0 a\sin\theta$.

The normalized *E*-plane and *H*-plane principal linear polarized patterns for the circular waveguide, are shown in Fig. 5.2.2.2. The corresponding co- and cross-polarized patterns in the $\varphi = 45°$ is also analyzed using Matlab and presented in Fig. 5.2.2.3.

The approximate circular waveguide feed pattern for *TE11* mode given by

$$e(\theta_0) = (1 + 0.81\cos\theta_0)\frac{J_1(\pi\sin\theta_0)}{\sin\theta_0}$$

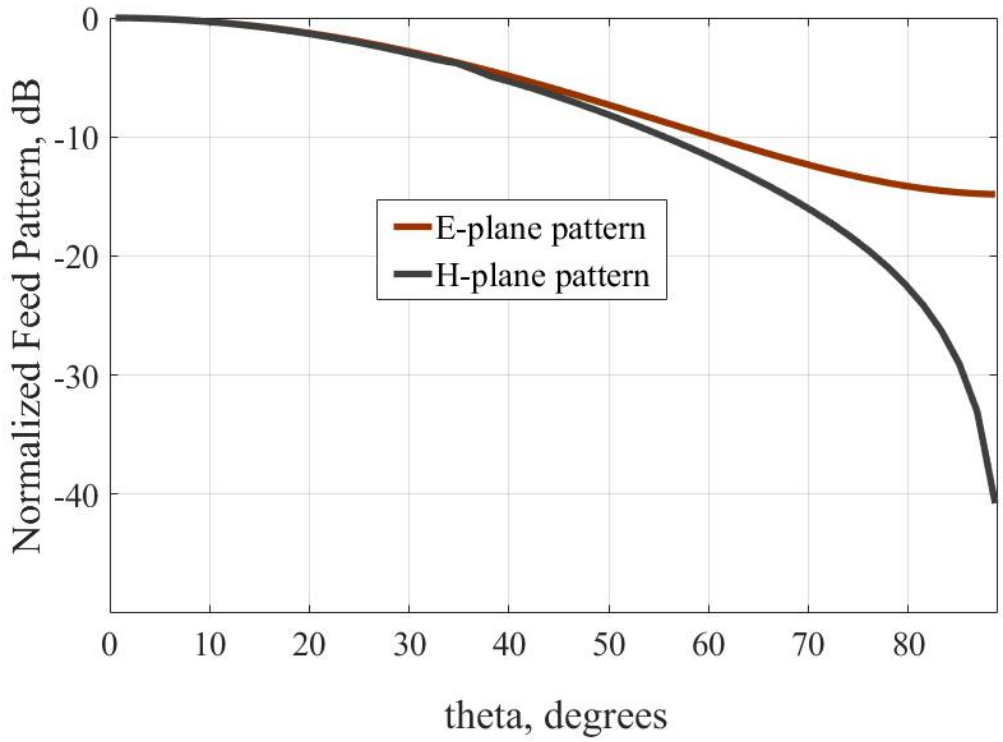

Fig. 5.2.2.2 E-plane and H-plane normalized radiation pattern of the circular waveguide TE_{11} horn antenna generated in MATLAB.

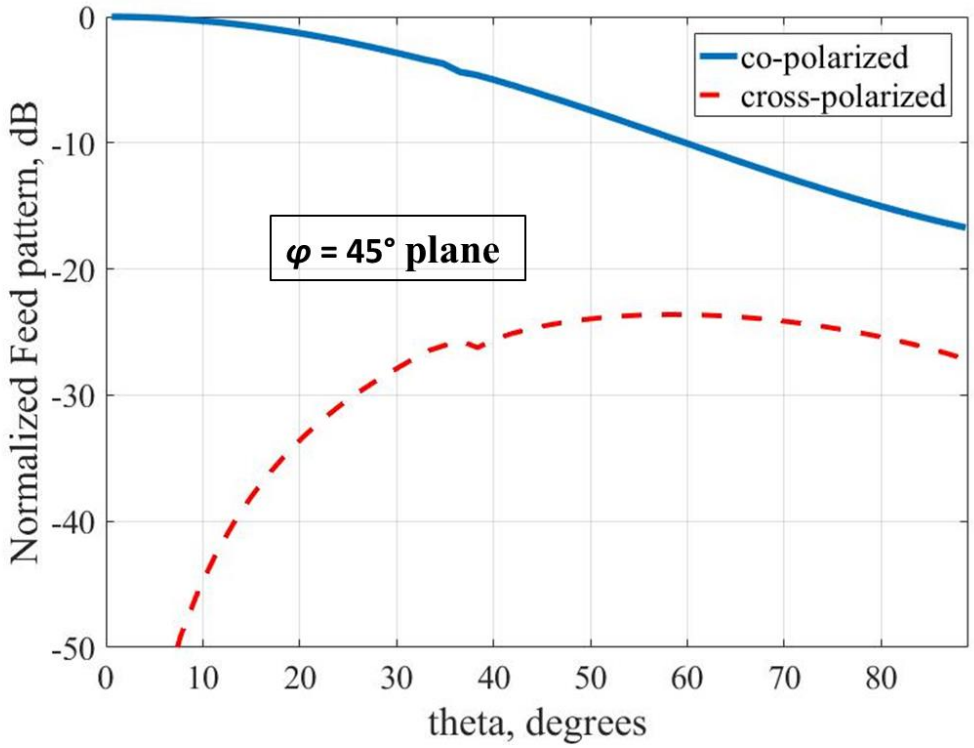

Fig. 5.2.2.3 Normalized radiation pattern of the circular waveguide TE_{11} horn antenna in φ = 45° plane showing co- and cross-polarized pattern generated in MATLAB.

The relative field profile for the TE_{11} circular waveguide is shown in Fig. 5.2.2.4. The field distribution at the projected aperture of the parabolic reflector antenna is shown in Fig. 5.2.2.5. The dense region shows the stronger field distribution on the reflector surface and it can be seen that the fields are *y*-polarized.

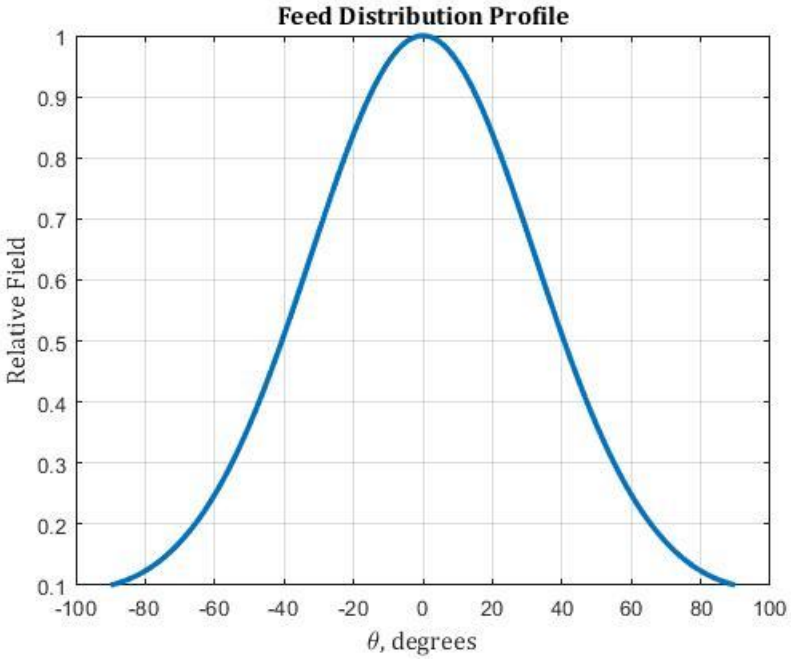

Fig. 5.2.2.4 Relative field of the TE_{11} feed source generated in MATLAB.

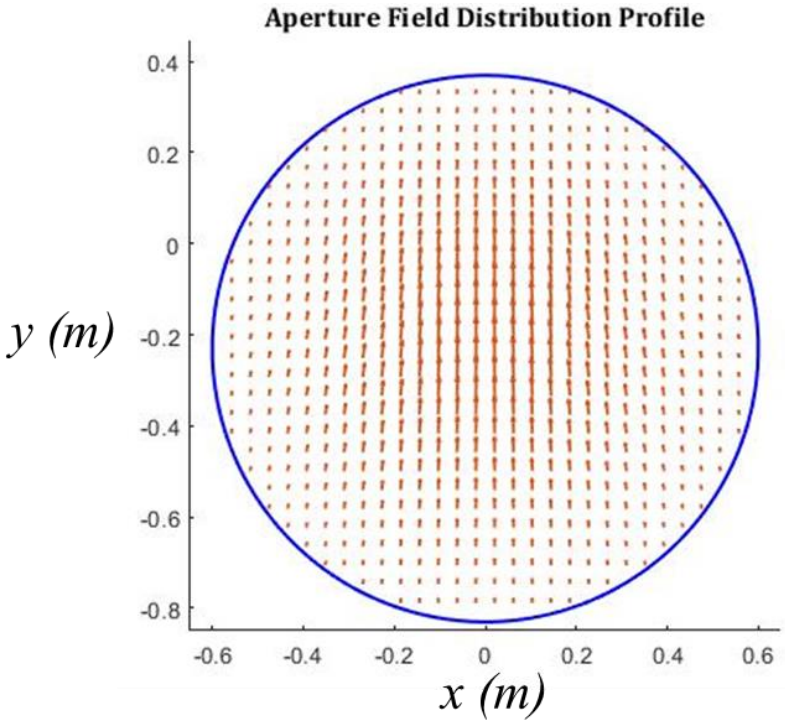

Fig. 5.2.2.5 Aperture field distribution profile of the offset reflector antenna generated in MATLAB.

It is determined through the GO analysis that the gain of the offset fed parabolic reflector is 42.41 dBi and the total efficiency of the reflector antenna is 76.6 %. The *H*-plane normalized radiation pattern of the reflector antenna analyzed using GO in MATLAB is shown in Fig. 5.2.2.6.

For the comparison purpose, the reflector with the same specification is also analyzed in Ticra GRASP using PO and the normalized radiation pattern is presented in Fig. 5.2.2.7. It can be seen that both the GO and PO analysis give us similar results. The peak directivity with PO analysis is 42.32 dBi and the maximum relative cross-polarization level is 23 dB.

Appendix shows the MATLAB code for GO analysis for a linear polarized feed source for an offset reflector.

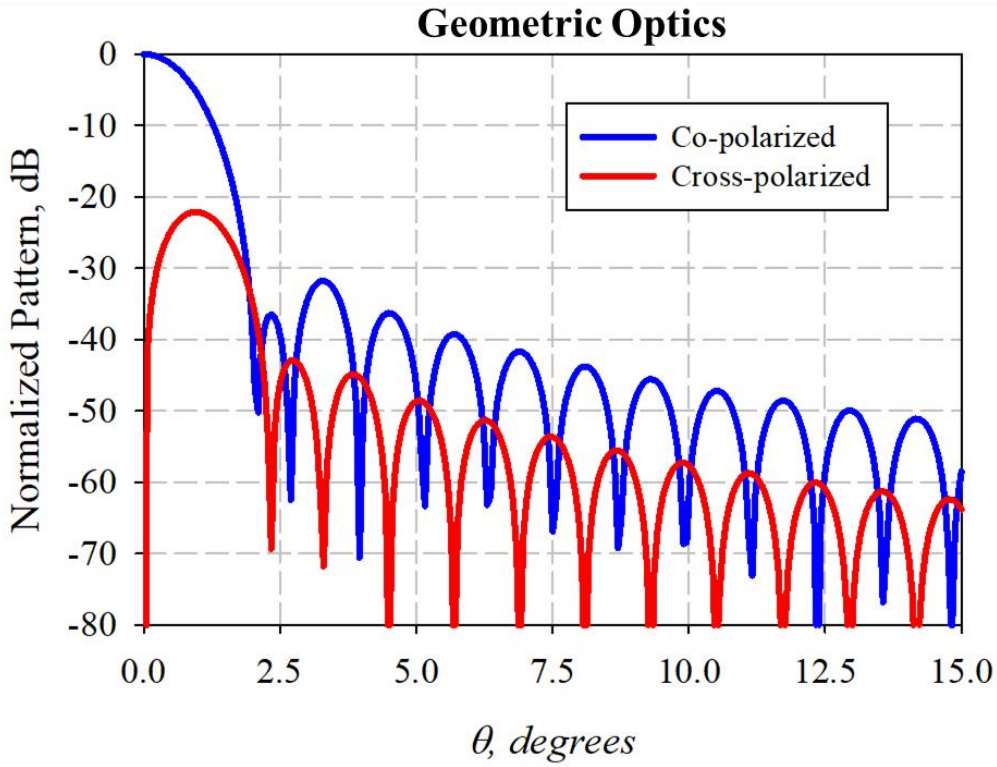

Fig. 5.2.2.6 *H*-plane normalized radiation pattern of the reflector antenna showing the co-polarization and cross-polarization level generated in MATLAB with GO analysis.

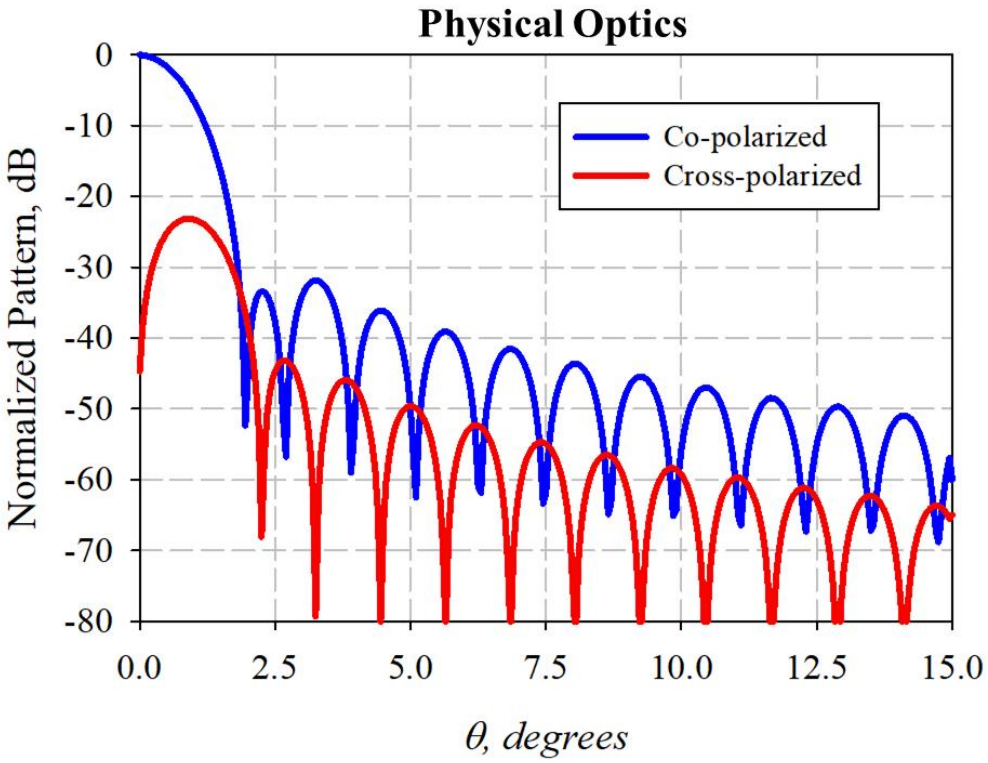

Fig. 5.2.2.7 *H*-plane normalized radiation pattern of the reflector antenna showing the co-polarization and cross-polarization level using Ticra GRASP with PO analysis.

5.2.3 Shooting and Bouncing Rays (SBR+)

The effect of CubeSat chassis on the integrated feed reflector assembly is analyzed in Ansys Savant. SBR+ is an advanced antenna performance simulation tool (Ansys Savant) that provides fast and accurate prediction of installed antenna patterns, near-fields and antenna-to-antenna coupling on electrically large platforms such as an example shown in Fig. 5.2.3.1. It analyzes installed antenna performance on platforms that are tens to thousands of wavelengths in size. It leverages the asymptotic Shooting and Bouncing Ray Plus (SBR+) technique to efficiently compute accurate solutions with incredible speed and scalability.

The state-of-the-art technology in HFSS SBR+ includes advanced physics models such as creeping waves, UTD diffraction rays and surface curvature extraction.

Hybrid Simulation: HFSS results for isolated antenna definitions can be imported and used to excite HFSS SBR+ simulations through application of the Equivalence Principle. This enables a smooth import of complex free-standing antenna models based on volume or surface meshing techniques. This can leverage precise results of isolated antenna simulations and capture the installed performance on full size aircraft, ships, vehicles or buildings with speed and accuracy.

The SBR algorithm implemented in Ansys Savant is summarized in the following steps:

1. Launch many rays from the transmit antenna toward the scattering geometry. The rest of the steps are for each ray.
2. Assign each ray a vector field weight according to the transmit polarimetric antenna pattern.
3. It has three important considerations
    a. If the ray escapes to space, ignore it.
    b. If the ray hits a surface, generate a reflected ray. Compute its fields according to the incident ray fields, the material properties of the surface, and GO principles.
    c. If the ray hits a penetrable surface, also generate a transmitted ray in the same direction as the incident ray and then extend and process it as one would do for the reflected ray.
4. At the ray hit-point, compute the incident and reflected field on the surface. Use these and the PO approximation to determine equivalent surface currents.
5. Radiate the equivalent currents to observation angles/points.
6. Continue tracing the reflected ray generated in step 3b and repeat from there. Likewise, for any transmitted ray generated in step 3c. Continue until either the ray escapes (Step 3a) or the maximum bounce limit is reached.

Step 5 is implemented with the following equation:

$$E_s(r) = \frac{1}{4\pi}\int_s ds' \left[(\hat{n}.\mathrm{E})\nabla\frac{e^{-jkR}}{R} + (\hat{n}\times\mathrm{E})\times\nabla\frac{e^{-jkR}}{R} - j\omega\mu(\hat{n}\times\mathrm{H})\frac{e^{-jkR}}{R} \right] \qquad (5.2.3.1)$$

where *Es* is the scattered electric field at the observation point, *S'* is the domain of the ray tube at the hit point and projected onto the surface.

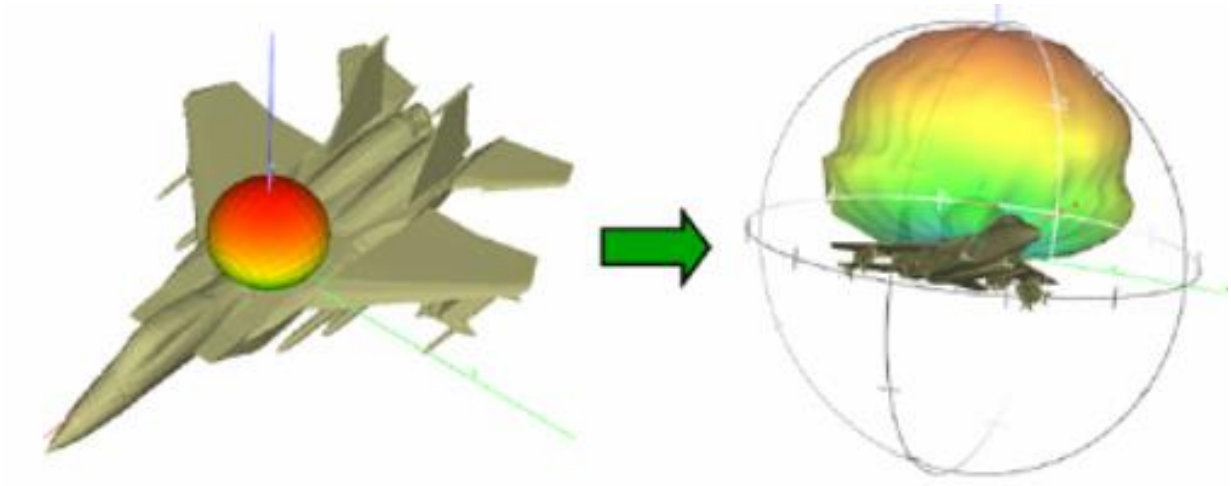

Fig. 5.2.3.1 Illustration of an application of SBR+ in determining the radiation performance of the antenna on an aircraft using Ansys Savant. [Online: https://www.ansys.com/products/electronics/ansys-savant-technical-features].

5.3 Sequential Nonlinear Programming Optimization Method

Ansys HFSS is used to optimize the proposed feedhorn based on the optimization method of Sequential Nonlinear Programming (SNLP). It is for the numerical solution of constrained nonlinear optimization problems of the form

$$\text{minimize } f(x) \text{ over } x \in \mathbb{R}^n \tag{5.3.1}$$

$$\text{subject to } h(x) = 0 \tag{5.3.2}$$

Sequential quadratic programming is an iterative procedure which models the nonlinear programming (NLP) for a given iteration x^k, by a Quadratic Programming (QP) sub-problem. It solves the QP sub-problem, and then uses the solution to construct a new iteration x^{k+1}. This construction is done in such a way that the sequence (x^k) converges to a local minimum x^* of the NLP (5.3.1)-(5.3.2) as $k \to \infty$.

- The method has a theoretical basis that is related to
    1. The solution of a set of nonlinear equations using Newton's method.
    2. The derivation of simultaneous nonlinear equations using Kuhn-Tucker conditions to the Lagrangian of the constrained optimization problem.

The Lagrange function, L **(X**,λ**),** corresponding to the problem of the above equation is given by:

$$L = f(\mathrm{X}) + \sum_{k=1}^{p} \lambda_k h_k(\mathrm{X}) \tag{5.3.3}$$

where λ_k is the Lagrange multiplier for the kth equality constraint.

The Kuhn-Tucker necessary conditions can be stated as:

$$\nabla L = 0 \text{ or } \nabla f + \sum_{k=1}^{p} \lambda_k \nabla h_k = 0$$

$$h_k(X) = 0, \qquad k = 1, 2, \ldots, p \tag{5.3.4}$$

where [A] is an $n \times p$ matrix whose kth column denotes the gradient of the function h_k. The above equations represent a set of $n+p$ nonlinear equations in $n+p$ unknowns (x_i, $i=1,...,n$ and λ_k, $k=1,...,p$).

Thus, we obtain:

$$\begin{bmatrix} [\nabla^2 L] & [H] \\ [H]^T & [\varnothing] \end{bmatrix}_j \begin{Bmatrix} \Delta X \\ \Delta\lambda \end{Bmatrix}_j = -\begin{Bmatrix} \nabla L \\ h \end{Bmatrix}_j \quad \text{with} \quad \begin{matrix} \Delta X_j = X_{j+1} - X_j \\ \Delta\lambda_j = \lambda_{j+1} - \lambda_j \end{matrix} \tag{5.3.5}$$

The above equation can be solved to find the change in the design vector $\Delta\mathbf{X_j}$ and the new values of the Lagrange multipliers, λ_{j+1}. The iterative process indicated by the above equation can be continued until convergence is achieved.

6 Proposed Feedhorn Requirements

The proposed horn antenna is developed as a feed for illuminating a compact offset parabolic reflector for 6U CubeSat (10 cm × 20 cm × 30 cm) application. The feed horn and reflector assembly take around 1U CubeSat volume. Fig. 6.1 illustrates the orthographic representation of the offset parabolic reflector antenna configuration. The stringent space constraint led to the selection of a small *f/D* of 0.25 to accommodate the reflector of diameter *D* = 10 cm inside the 1U block of the CubeSat. Accordingly, the clearance *H* is taken to be zero to avoid extension of the feed horn and reflector assembly beyond the allotted volume. Interested readers are referred to [2, 37] for the well-known operating principle of an offset parabolic reflector antenna.

The above constraints on the parameter value resulted in the half cone angle subtended at the rim of the reflector ψ_e, to be 63.44° as given in (6.1). Also, the feed source needs to be directed towards the center of the offset reflector from the focal axis by an angle ψ_f = 90° as equated in (6.2) [37].

$$\psi_e = \tan^{-1}\frac{2fD}{4f^2 + H(\mathrm{D}+\mathrm{H})} = 63.44^\circ \qquad (6.1)$$

$$\psi_f = 2\tan^{-1}\frac{2H + D}{4f} = 90^\circ \qquad (6.2)$$

As a result, the proposed feed horn antenna is designed to have a 12 dB half edge illumination of around 64° within the desired bandwidth of 79 GHz to 88 GHz. The ray tracing diagram of an offset parabolic reflector with these obtained values is plotted using Ticra GRASP and is shown in Fig. 6.2.

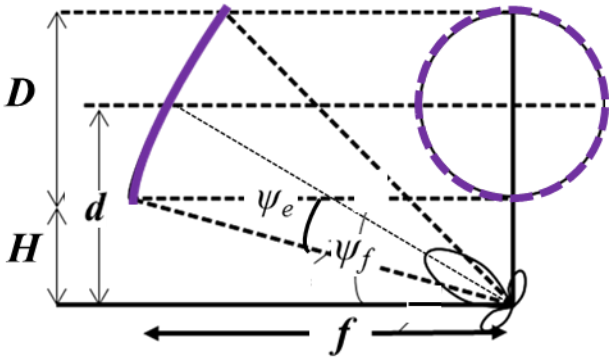

Fig. 6.1 Parameters of an offset fed parabolic reflector in an orthographic representation.

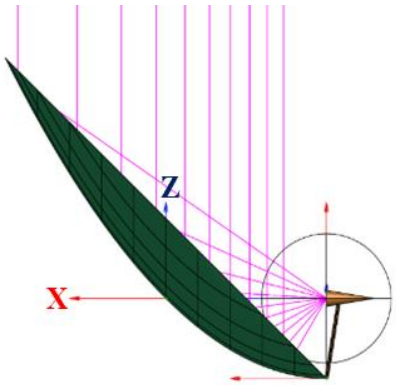

Fig. 6.2 Ray tracing diagram using Ticra GRASP with ψ_e = 63.44° and ψ_f = 90° for an offset parabolic reflector with *f/D* = 0.25.

To study the effect of strict physical constraints on the co- and cross-polarization performance of the antenna, an ideal simulation with the Gaussian left-hand circular polarization (LHCP) feed source is carried in GRASP. Ideal Gaussian feed assumes that the cross-polarization level is below -200 dB. The peak RHCP directivity of the offset parabolic reflector illuminated by the ideal Gaussian LHCP feed is 37.5 dBic and the cross-polarization separation is 41.5 dB within the main lobe at 86 GHz as presented in Fig. 6.3. The 3dB beamwidth is 2.3° and the spillover loss of the offset reflector is 0.63 dB at 86 GHz. Spillover radiation occurs at 45° which is the angle of orientation of the reflector with respect to the boresight of the feed horn. The spillover loss could be reduced by increasing the *f/D* ratio. However, *f/D* ratio is limited by the volume constraint of the CubeSat. Thus, significant cross polarization is observed with the ideal feed illumination of the reflector. This high cross polarization effect is the limitation of the low *f/D* ratio and will be present even with the proposed feed horn and reflector as discussed in section IV.

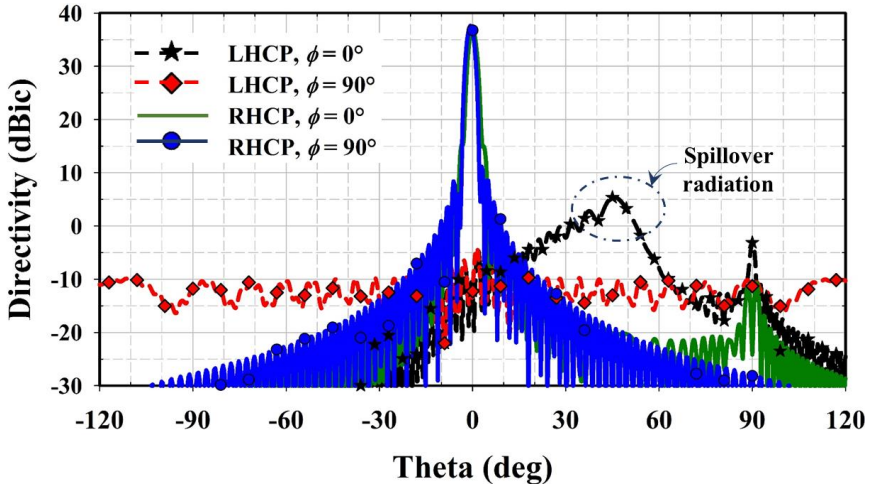

Fig. 6.3 Simulated directivity pattern of an ideal Gaussian fed offset parabolic reflector with *f/D* = 0.25 in Ticra GRASP.

7 Inbuilt Feedhorn Polarizer

7.1 Proposed Feed Horn Antenna Geometry (Initial Design)

Circular polarization is achieved by incorporating a polarizing structure inside the cylindrical waveguide. Fig. 7.1.1(a) and (b) show the front view and the split view geometry in YZ plane of the proposed feed horn antenna. The inbuilt polarizing structure employs nine pairs of circular cavities in the cylindrical waveguide wall as shown in Fig. 7.1.1(b). These cavities are at 45° with respect to the rectangular input port. The horn is designed using circular waveguide section of 1.0 mm thick aluminum with an overall length of 26 mm, and the aperture diameter of 3.26 mm. The cavity diameter, *d* is 1.39 mm and the spacing between the cavity pairs, *s* is 1.7 mm.

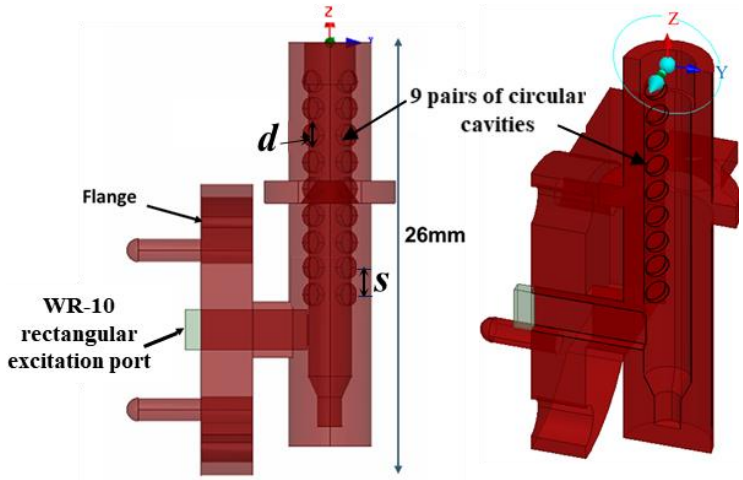

(a) (b)

Fig. 7.1.1 Proposed LHCP feed horn antenna geometry (a) front view and (b) split plane view.

The waveguide section below the polarizing structure is around λ/4 in length and helps in the suppression of any spurious modes. In addition, tapered waveguide backshort section improves the impedance matching. The proposed inbuilt polarizer has the advantage of reducing the degradation in the antenna radiation performance from fabrication inaccuracy because the cavities are placed on the wall of the circular waveguide where the electromagnetic field is sparse as opposed to placing metallic pins [3] in the dense electromagnetic field region inside the circular waveguide. The number of cavities, diameter of the cavities and the spacing of the cavities are the design parameters which can be tuned to optimize the overall impedance matching and the axial ratio bandwidth.

7.2 Principle of Operation and Parametric Study

The principle of CP generation is explained for the inbuilt polarizer section of the proposed feed horn antenna. Fig. 7.2.1 shows the two-port model of the polarizer section of the feed horn. Since the input is 45° offset with respect to the cavity pairs, the input RF signal E_{inc} splits into two orthogonal degenerate TE_{11} modes. The propagation constant of these propagating modes is

different due to the cavity pairs along E_{out1} as shown in Fig. 7.2.2. As a result, the E_{out1} field in the direction of the cavity pairs gets an additional phase delay of $\lambda/4$ relative to the orthogonal field E_{out2} at the aperture of the polarizer to generate the desired LHCP. The polarizer device can be considered as a three port structure even with its two physical ports. The two degenerate modes at the output circular wave-port makes the polarizer as a three port structure. The general expression for the 3 × 3 scattering matrix for the proposed polarizer is written as (7.2.1).

$$S = \frac{1}{2}\begin{bmatrix} 0 & -\sqrt{2}\cdot e^{-j\beta_1 L} & \sqrt{2}\cdot e^{-j\beta_2 L} \\ -\sqrt{2}\cdot e^{-j\beta_1 L} & 0 & 0 \\ \sqrt{2}\cdot e^{-j\beta_2 L} & 0 & 0 \end{bmatrix} \tag{7.2.1}$$

where L is the length of the circular waveguide polarizer and β_1, β_2 are the propagation constants in the polarizer. The summation of the difference in propagation constants of the two modes $\beta_1(z_i, f)$ and $\beta_2(z_i, f)$ along the length of the polarizer gives the phase difference of 90° [4], as shown in equation (7.2.2),

$$\sum_{i=1}^{L/\delta z} \left(\beta_2(z_i, f) - \beta_1(z_i, f)\right)\delta z = \frac{\pi}{2} \tag{7.2.2}$$

where z_i (along z direction) is the distance from the feed point for the ith discretized section in the waveguide at frequency f.

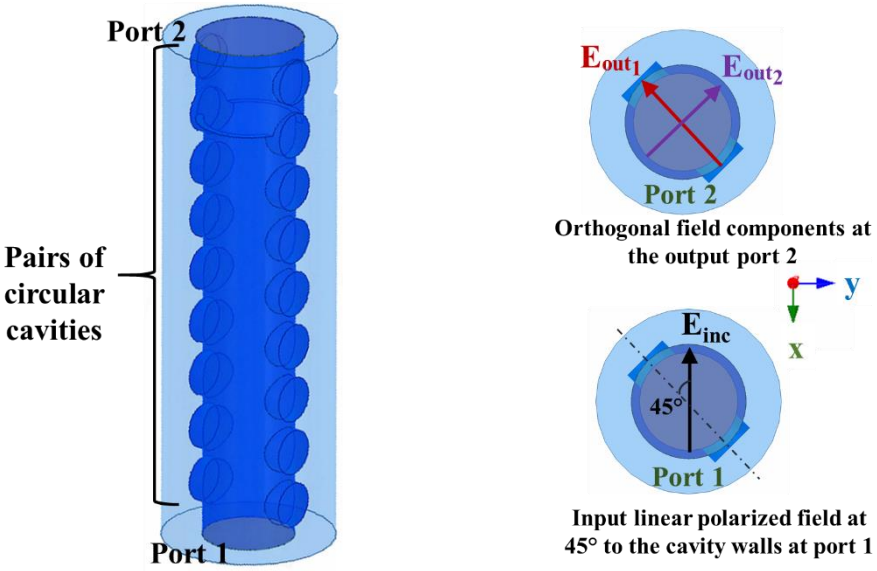

(a) (b)

Fig. 7.2.1. Two-port model of polarizer structure of the proposed antenna (a) front view and (b) top view showing input and output field components.

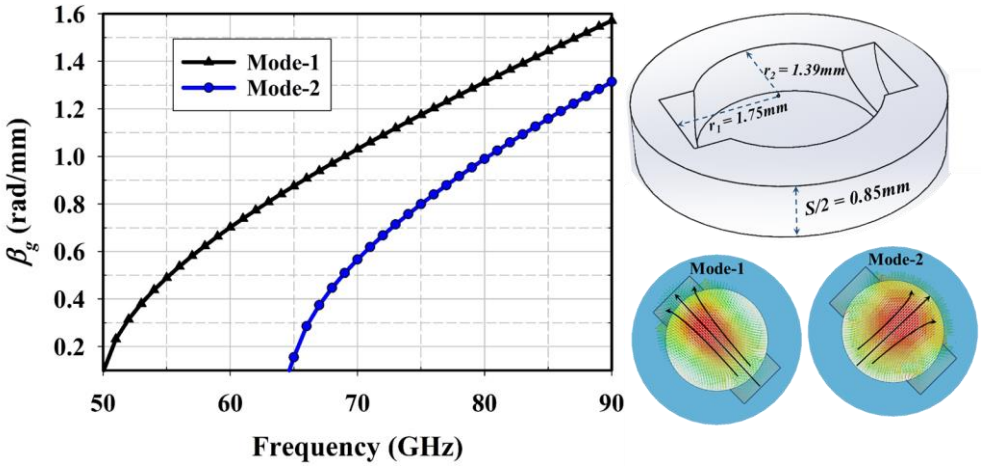

Fig. 7.2.2. Dispersion relation graph for a section of the polarizer simulated in Ansys HFSS.

The effect of the presence of circular cavities in the polarizer section is analyzed using Ansys HFSS. Without the circular cavities, the section acts as a regular cylindrical waveguide and the linear polarized wave is observed at the output port as illustrated in Fig. 7.2.3 (a). With the proposed optimized design of 9 pairs of circular cavities and cavity diameter d = 1.39 mm, the field component E_{out1} experiences additional phase lag of 90°. Also, the amplitude of the two orthogonal field components is same leading to the generation of LHCP wave at the output port as shown in Fig. 7.2.3(b).

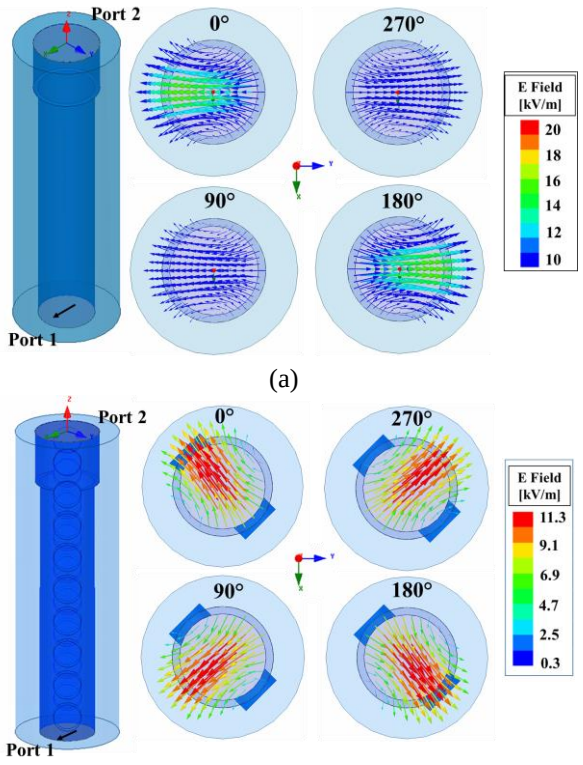

Fig. 7.2.3 Effect of circular cavities on the *E*-fields in the polarizer section (a) no cavity pairs leading to linear polarization and (b) 9 cavity pairs leading to circular polarization.

A parametric analysis is carried out on the number of circular cavity pairs, diameter, depth and spacing between the circular cavities keeping the length of the feed horn constant to determine the optimum value of the parametric variables. Later, based on the optimum parametric values, sequential nonlinear programming (gradient) optimization method is employed on the feed horn with the goal of AR less than 1.5 dB within the frequency range of 79 GHz to 88 GHz. The effect of number of circular cavity pairs on the amplitude and phase difference between the two orthogonal field components is shown in Fig. 7.2.4. It is seen that for nine pairs of circular cavities, the phase difference between the output field components is 90° (±15°) and the maximum amplitude imbalance is 0.10 dB.

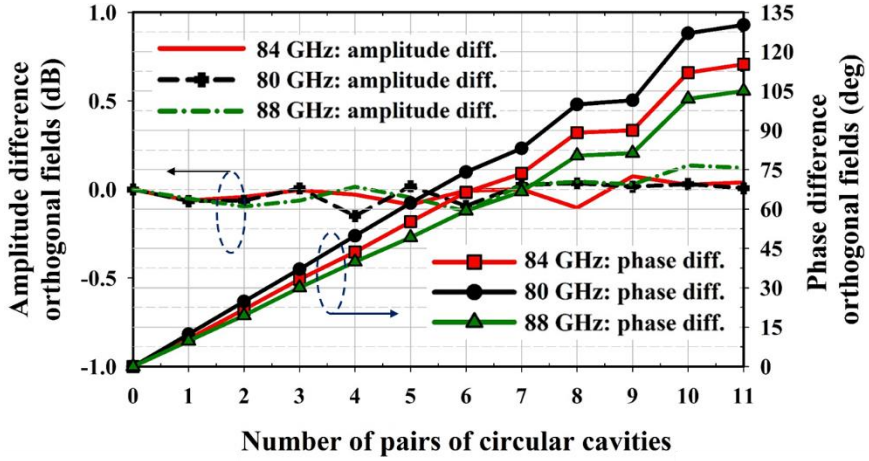

Fig. 7.2.4. Amplitude and phase difference between the two orthogonal field components at the output port of the polarizer as a function of number of circular cavities pairs.

Fig. 7.2.5(a) presents the effect of varying the cavity diameter on the output phase difference between the field components as a function of frequency for nine pairs of circular cavities. It is clear that for cavity diameter d = 1.39, the phase difference between the output field components is around 90°. The effect of different spacing s between the cavities on the phase difference is shown in Fig. 7.2.5(b). The spacing s = 1.70 mm provides the phase delay of 90° (± 10°) between the output field components.

Hexagonal, square and triangular are the three different shapes of the cavity that are studied in addition to the circular cavity shapes as illustrated in Fig. 7.2.6. The effect of different cavity shapes on the phase difference is shown in Fig. 7.2.7. The triangular cavity polarizer provides the least phase delay, whereas the proposed circular cavity polarizer offers the optimum phase difference to generate CP.

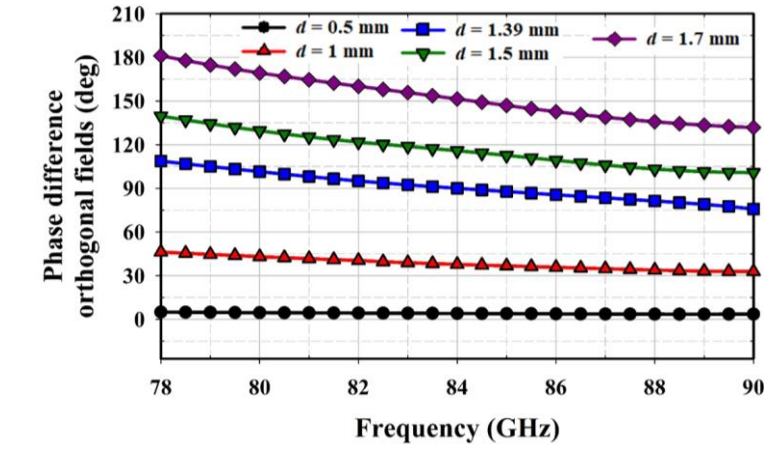

(a)

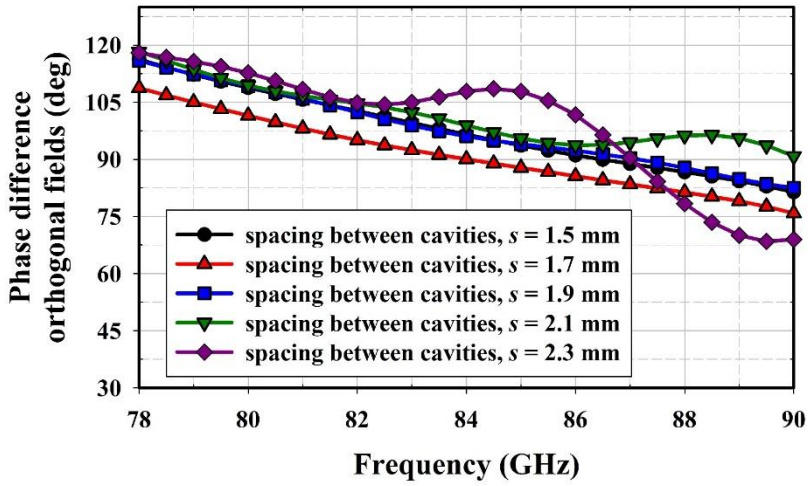

(b)

Fig. 7.2.5. Effect of different (a) cavity diameter =*d* and (b) spacing = *s* between the cavities, on the phase difference between the two orthogonal fields at the output port of the polarizer.

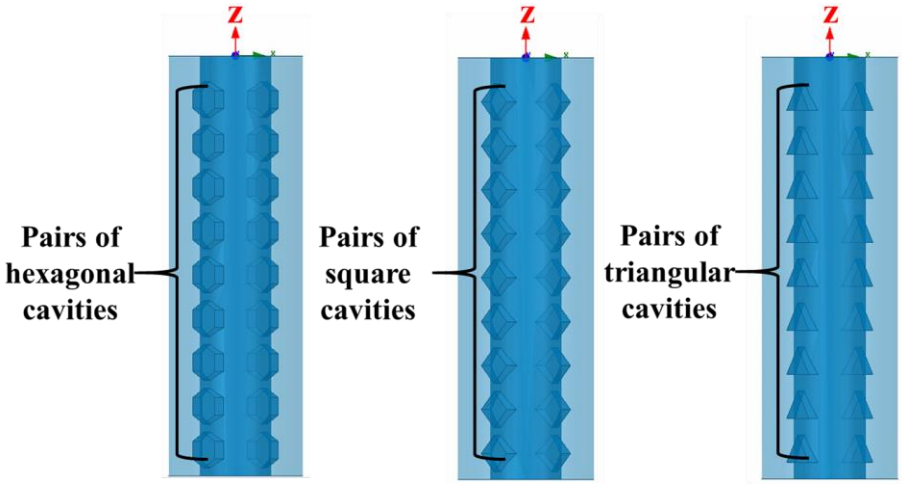

(a) (b) (c)

Fig. 7.2.6. Different cavity shapes in the polarizer (a) hexagonal, (b) square and (c) triangular cavity shapes.

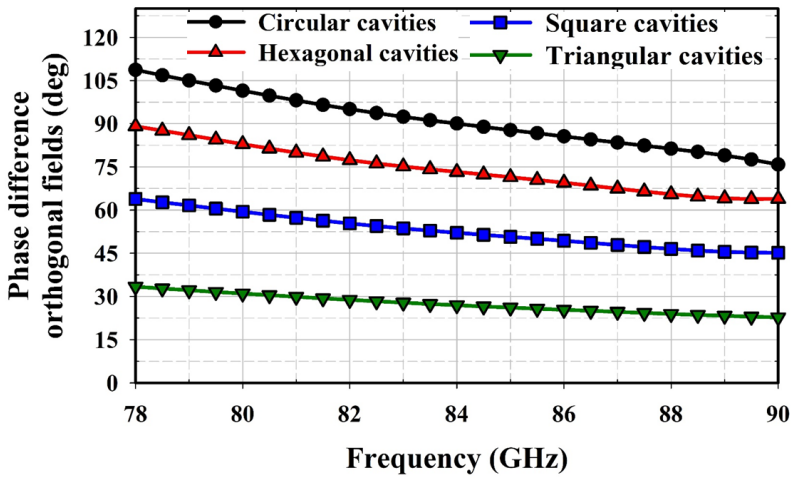

Fig. 7.2.7. Effect of different shapes of the cavity on the phase difference between the two orthogonal fields.

7.3 Modified Designs for Ease of Fabrication

The initial proposed design of Fig. 7.1.1 needs to be modified for the ease of fabrication. Extra aluminum thickness is added to the walls of the initial horn antenna for structural rigidity. Two different modified designs are studied with the additional metal thickness with split plane waveguide construction, which allows in easier fabrication in machining through CNC technology.

Fig. 7.3.1 shows the CAD rendering of the modified design #1 with rectangular wall around the cylindrical horn antenna. The overall thickness of the aluminum wall is 5.25 mm. The rectangular metal wall creates asymmetry in the feed aperture which results in higher diffraction around the wall edges. A final modified design is proposed as shown in Fig. 7.3.2 which includes a 1.4 mm thick circular skirt at the top of the rectangular wall to make the aperture symmetric and mitigate the diffraction current. The physical dimension of the optimized horn antenna is 26 mm × 14 mm × 5.25 mm which corresponds to the electrical dimension of 7.2λ × 3.9λ × 1.4λ at 84 GHz. The optimum cavity diameters are $d_1 = d_2 = d_9 = 1.40$ *mm*, $d_3 = d_4 = d_7 = d_8 = 1.35$ *mm, and* $d_5 = d_6 = 1.30$ *mm*. The spacing between the cavity pairs are $s_1 = s_2 = s_3 = s_5 = s_7 = s_8 = 1.70$ *mm*, $s_4 = 1.60$ *mm, and* $s_6 = 1.80$ *mm*, and the depth of the cavity is 0.36 mm.

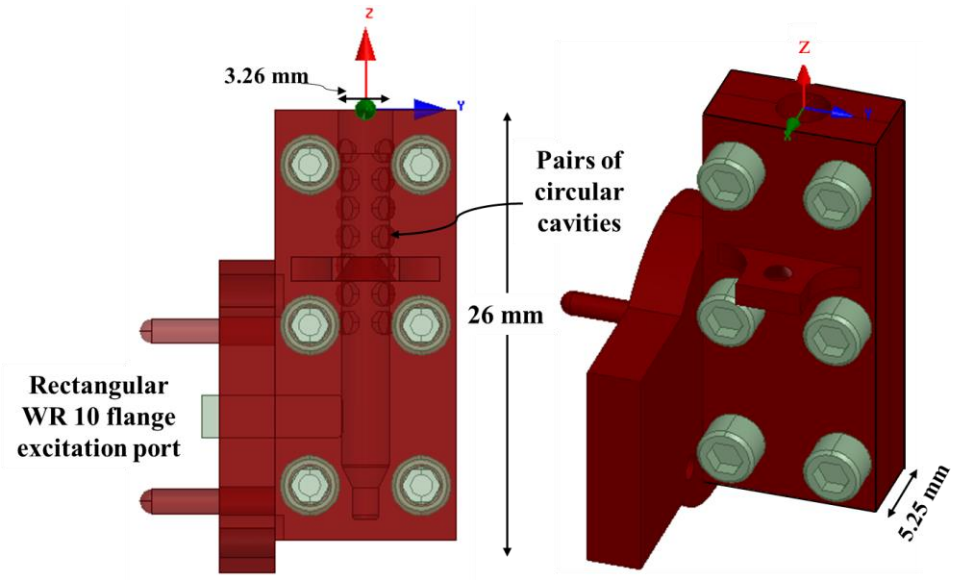

(a) (b)

Fig. 7.3.1 Modified design #1 with extra metal thickness around the antenna walls for ease of fabrication (a) front view and (b) isometric view.

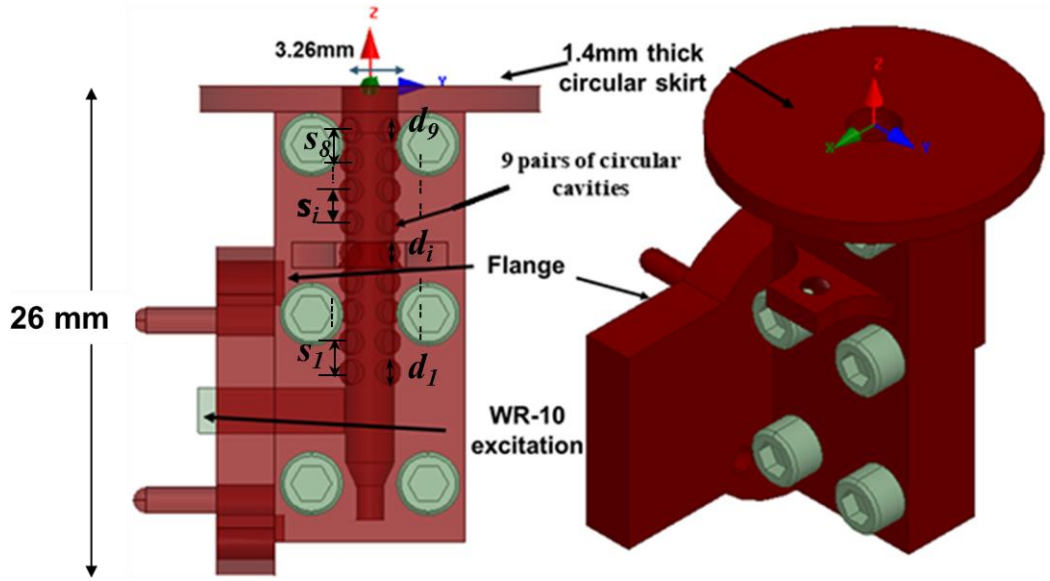

(a) (b)

Fig. 7.3.2. Final optimized modified design with circular skirt (a) front view and (b) isometric view.

The simulated impedance matching performances of the modified design #1 and the final optimized designs are presented in Fig. 7.3.3. Both the designs offer wideband matching (S_{11} below -15 dB) from 79.5 GHz to 88 GHz. The circular polarization purity is affected by the asymmetric aperture wall of the modified design #1 as observed in the AR plot of the two designs presented in Fig. 7.3.4. The final optimized design shows an excellent AR below 1.2 dB over the entire matching bandwidth. The 3 dB AR beamwidth of the modified design #1 is 61°, 85°, and 82° and for the final modified design is 90°, 91°, and 108° as shown in Fig. 7.3.5 for three

frequencies in the matching bandwidth at 79 GHz, 83 GHz, and 86 GHz, respectively. The final optimized design has a superior AR performance over a wide angle and also shows symmetric behavior in the elevation plane.

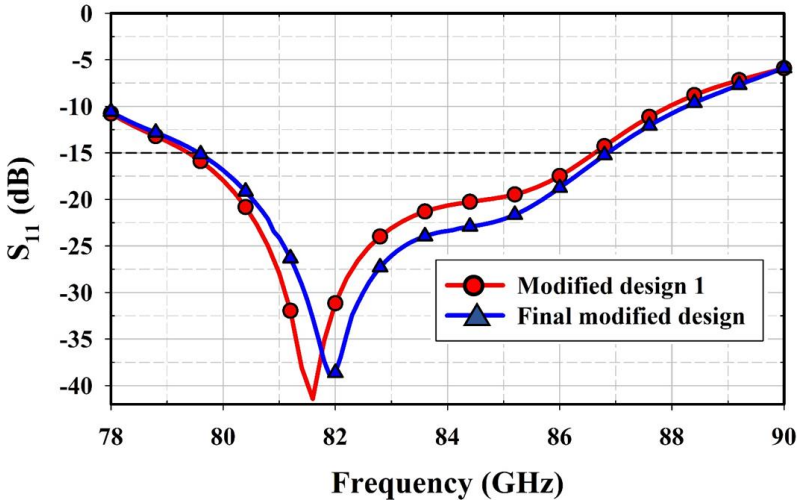

Fig.7.3.3 Simulated reflection coefficient of the feed horn with modified design #1 and final modified design.

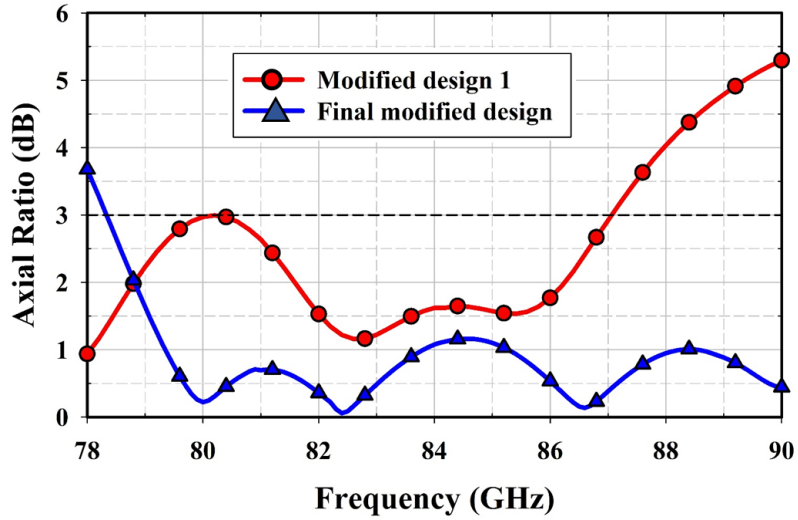

Fig. 7.3.4 Simulated axial ratio of the feed horn with modified design #1 and final modified design as a function of frequency.

Fig. 7.3.6 shows the 2D normalized radiation pattern at $\varphi = 0°$, $\varphi = 45°$, and $\varphi = 90°$ for the modified design #1 and final optimized design at 79 GHz, 83 GHz, and 86 GHz. The diffraction from the edges of the rectangular wall is stronger in the modified design #1. This results in higher ripples in the radiation patterns of the design #1 as shown in Fig. 7.3.6(a, c, e). The effect of ripples is stronger at lower frequency at 79 GHz as opposed to the higher frequency at 86 GHz because the currents travel longer paths at lower frequency resulting in more diffraction around the edges. The presence of circular skirt at the top of optimized design reduces the diffraction and leads to symmetric radiation pattern as shown in Fig. 7.3.6 (b, d, f). Thus, it is observed that the final optimized design provides stable and symmetric radiation pattern over the entire matching

bandwidth which satisfies the requirement of good feed source for reflector applications. The average cross-polarization separation is more than 25 dB for the final optimized feed horn over the desired matching bandwidth.

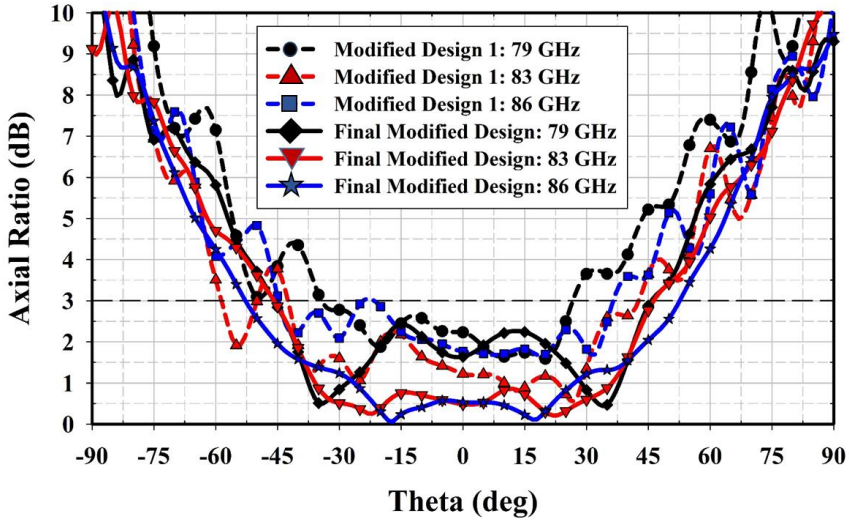

Fig. 7.3.5 Simulated axial ratio vs. elevation angle, theta, of the feed horn with modified design #1 and final modified design at 86 GHz.

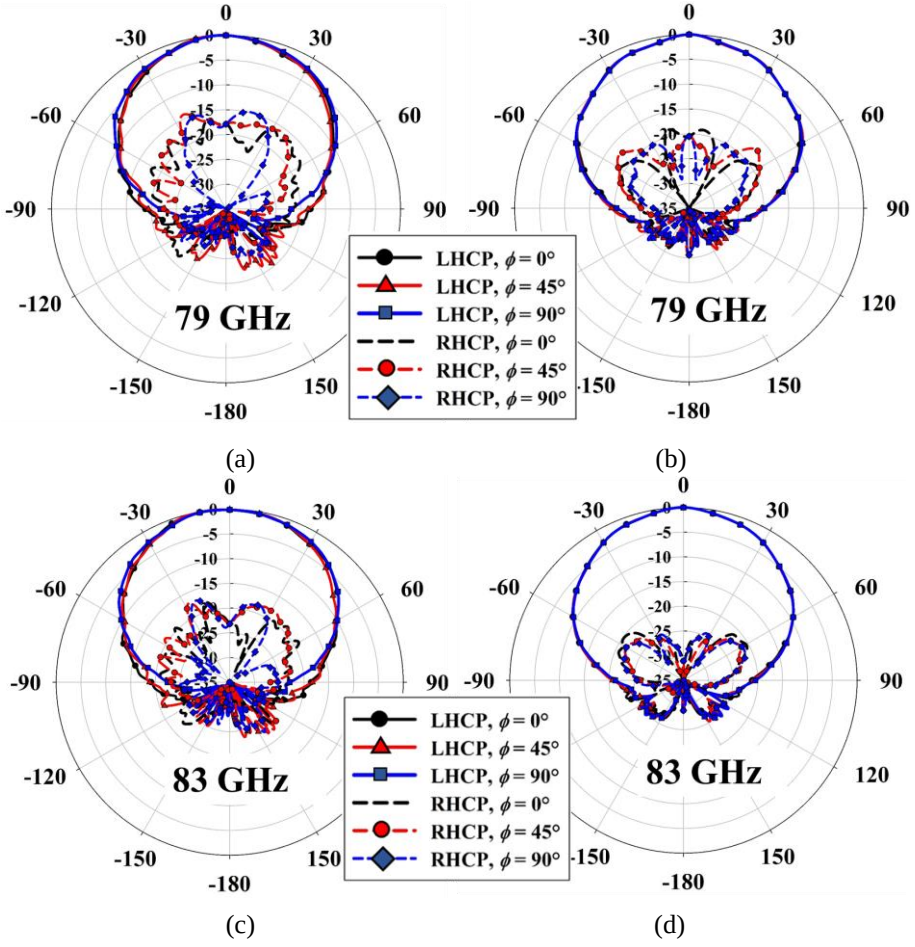

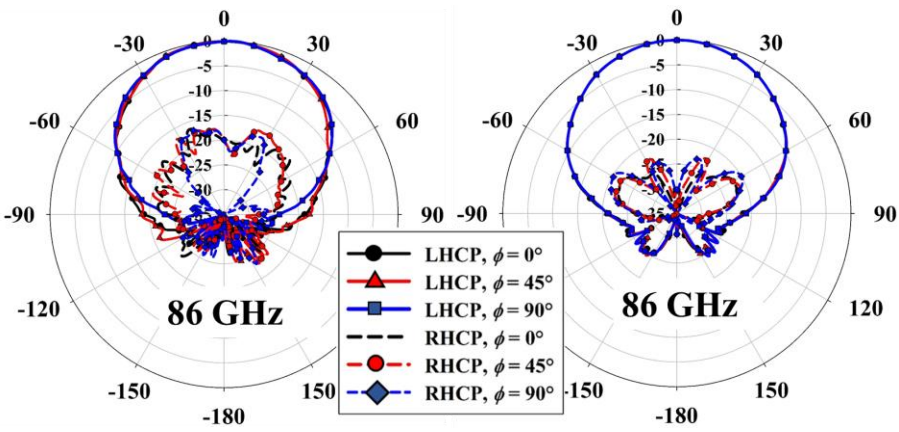

(e) (f)

Fig. 7.3.6 Simulated 2D normalized radiation pattern of the feed horn with modified design #1 (a, c, e) and final modified design (b, d, f).

The total simulated antenna efficiency is above 90% for both the designs from 79 GHz to 88 GHz as shown in Fig. 7.3.7. The peak LHCP gain as a function of frequency is also presented in Fig. 7.3.7. The average 12 dB half edge illumination beamwidth of the final optimized design is around 65° over the matching bandwidth. The optimized feed horn antenna is used as a feed to illuminate an offset reflector with small *f/D* = 0.25 as discussed in section 8.

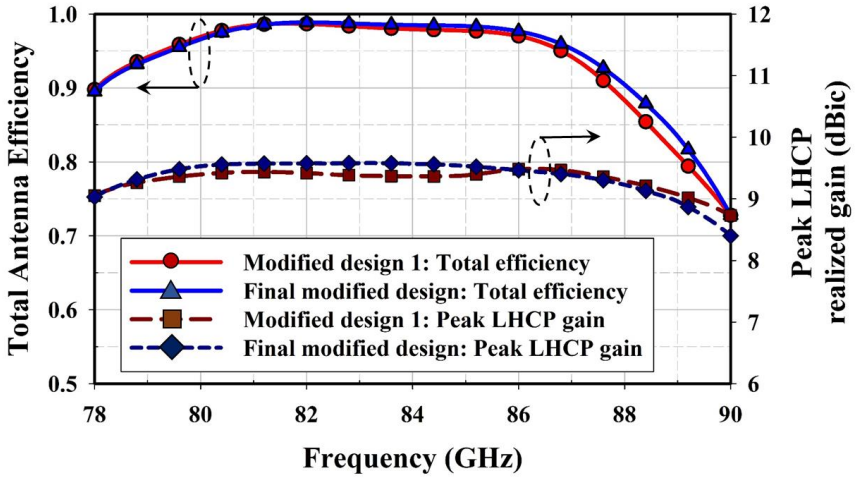

Fig.7.3.7 Simulated total antenna efficiency of the feed horn with modified design #1 and final modified design as a function of frequency.

7.4 Modified Feed Horn Integrated with Offset Parabolic Reflector

The proposed optimized feed horn antenna is used as a feed source to excite an offset parabolic reflector with a small *f/D* = 0.25, reflector diameter 10 cm and no feed clearance from the focal axis. Fig. 7.4.1(a) and (b) show front and side view rendering of the feed reflector geometry. Extra metal thickness is added around the rim of the reflector for ease of fabrication and structural support of the strut. The feed source is directed at an angle of ψ_f = 90° towards the center of the offset reflector from the focal axis as discussed in section II. The offset reflector was analyzed using Ticra GRASP which utilizes Physical Optics (PO) currents on the reflector and Physical

Theory of Diffraction (PTD) rim currents to obtain the total induced current on the reflector. The radiation from the feed horn and from the induced currents on the offset parabolic reflector are summed to obtain the total field.

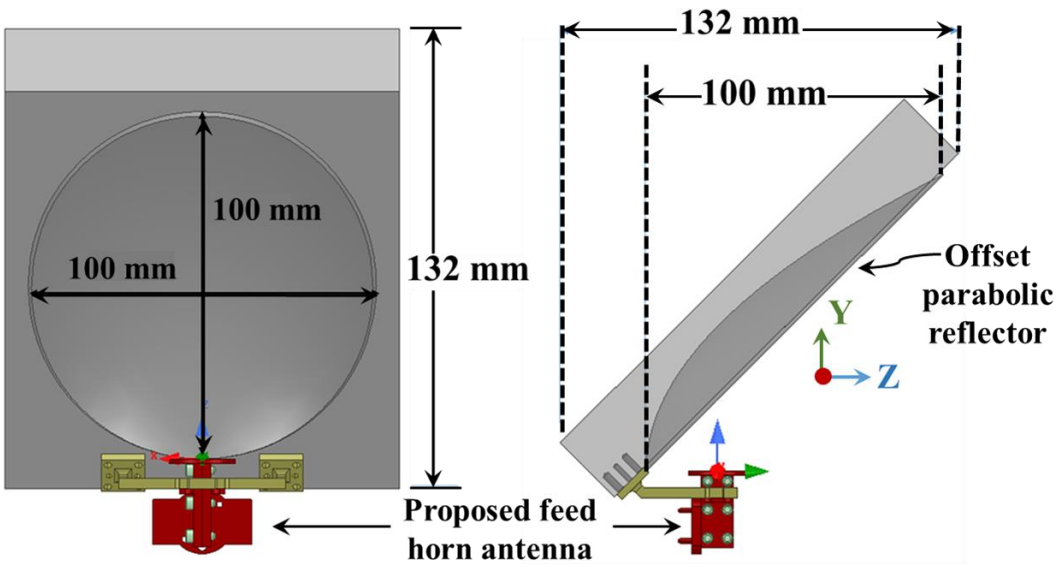

(a) (b)

Fig. 7.4.1. Offset parabolic reflector integrated with the proposed optimized feed horn antenna (a) front view (b) side view.

8 Simulation and Measurement Results of the proposed antenna

The proposed feed horn and the offset parabolic reflector antenna is fabricated at the Custom Microwave Inc., facility [38]. Fig. 8.1(a) and (b) are the photographs of the fabricated feed horn and the offset reflector integrated with the feed horn, respectively. The fabricated designs are measured at MVG spherical near-field chamber.

(a) (b)

Fig. 8.1. Photograph of the fabricated (a) proposed feed horn antenna and (b) the offset parabolic reflector with feed horn assembly.

The impedance matching bandwidth of the feed horn is (S_{11} below -15 dB) from 79.5 GHz to 88 GHz. The simulated and measured impedance matching of the feed horn antenna is in excellent agreement, and the measured impedance matching is maintained with the feed reflector assembly as shown in Fig. 8.2. The measured AR for the feed horn antenna is below 1.2 dB over the matching bandwidth, which is consistent with the simulation results as shown in Fig. 8.3. The simulated and measured polarimetric results for the AR as a function of elevation (step size $\Delta\theta$ = 1°) and azimuth ($\Delta\phi$ = 1°) angles are presented in Fig. 8.4(a-f) at 79 GHz, 83 GHz, and 86 GHz. The average simulated and measured 3dB AR beamwidth is around 100° within the desired frequency range. The slight variation in the measured and simulated results might be due to the fabrication tolerance of the cavities in the feed horn.

The simulated and measured 2D normalized radiation patterns of the proposed feed horn antenna is presented at 79 GHz, 83 GHz, and 86 GHz in Fig. 8.5. The measured results show excellent correlation with the simulated results in terms of beamwidth and symmetrical pattern. The 3D realized gain radiation pattern is shown for the simulation (a, c, e) and measurement (b, d, f) in Fig. 8.6. It can be observed that a stable and symmetric radiation pattern is obtained over the entire desired bandwidth. The simulated peak LHCP gain of the feed horn is 9.2 dBic, 9.5 dBic, and 9.45 dBic and the peak cross-polarization separation (separation between the peak co-polarization LHCP gain and the peak cross-polarization RHCP gain) is 20 dB, 24 dB, and 25 dB at 79 GHz, 83 GHz, and 86 GHz, respectively. The measured peak LHCP gain of the feed horn is 7.9 dBic, 8.9 dBic, and 9.1 dBic and the peak cross-polarization separation is 16 dB, 20 dB, and 19 dB at 79 GHz, 83 GHz, and 86 GHz, respectively. The discrepancy in the measured and simulated results might be due to fabrication and measurement tolerances. The measured peak LHCP gain and 12

dB half edge illumination beamwidth of the proposed feed horn antenna as a function of frequency is presented in Fig. 8.7.

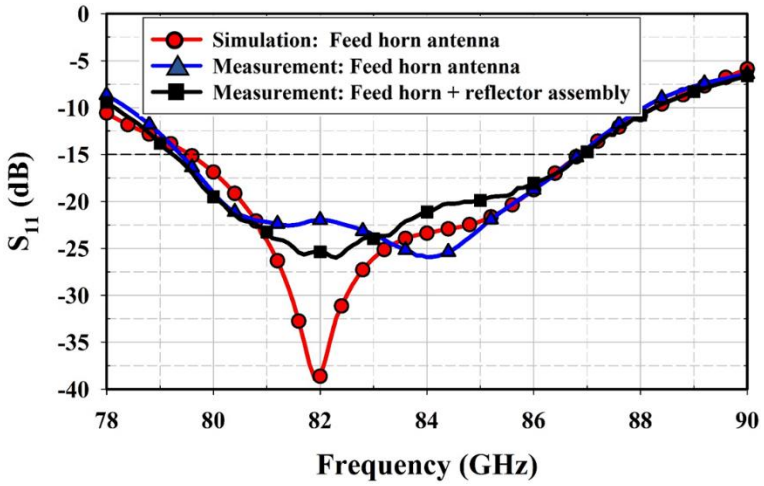

Fig. 8.2 Simulated and measured S_{11} of the proposed feed horn antenna and the measured S_{11} of the integrated feed horn and reflector antenna.

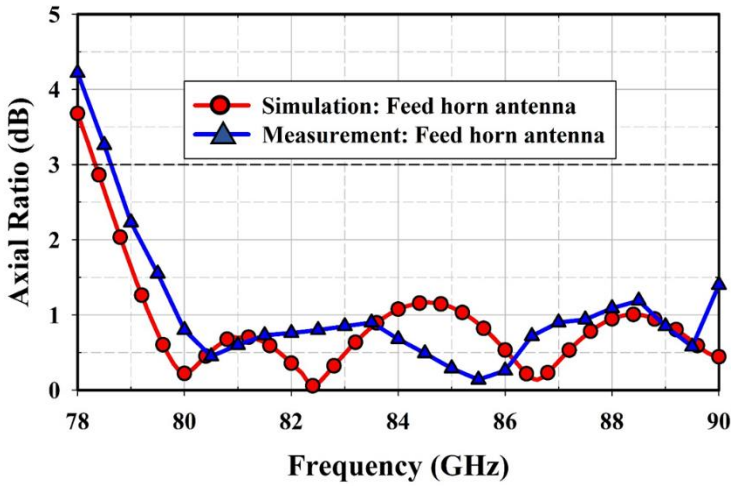

Fig. 8.3 Simulated and measured axial ratio of the proposed feed horn antenna as a function of frequency.

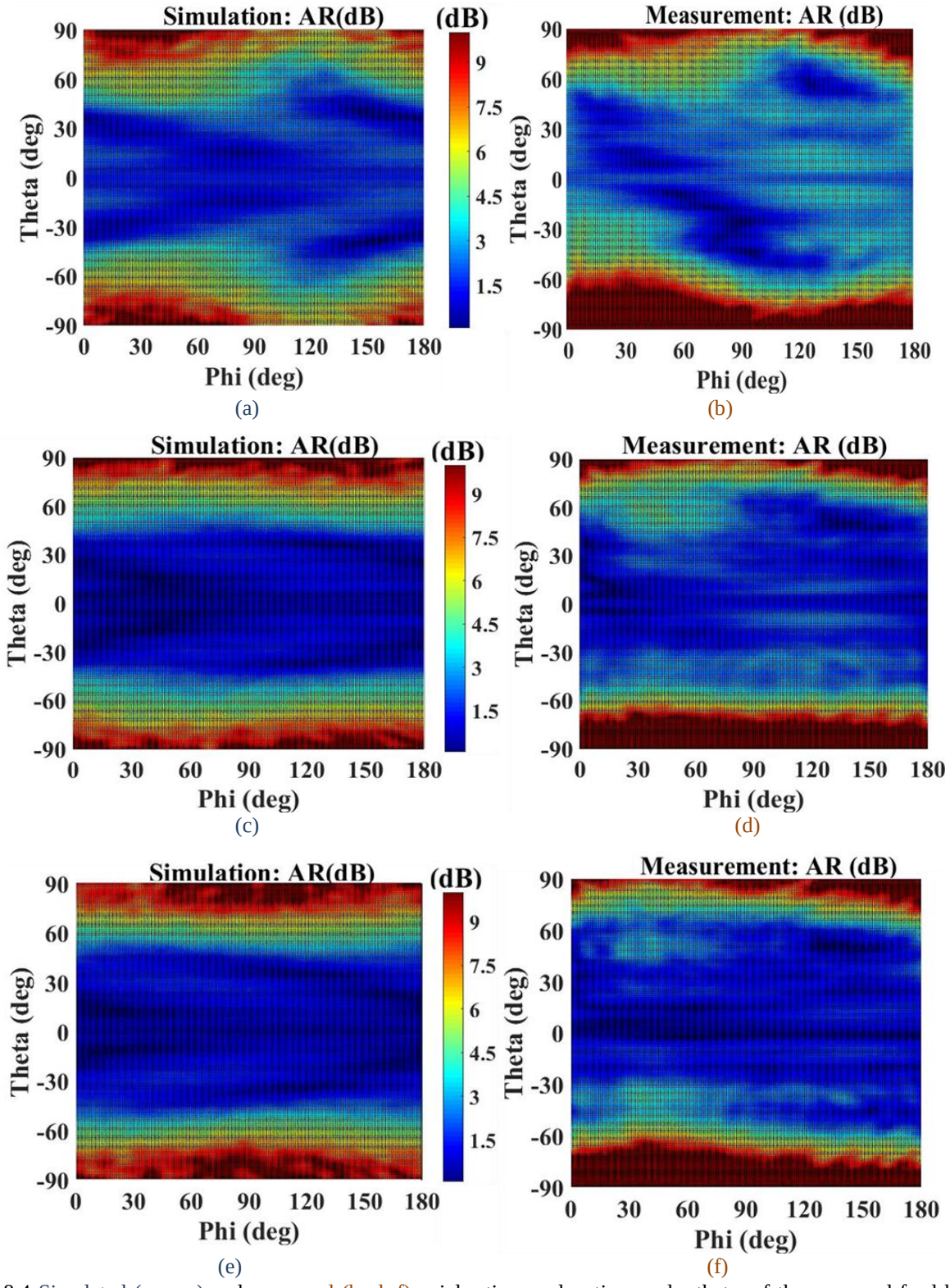

Fig. 8.4 Simulated (a, c, e) and measured (b, d, f) axial ratio vs. elevation angle, theta, of the proposed feed horn antenna at 79 GHz, 83GHz and 86 GHz.

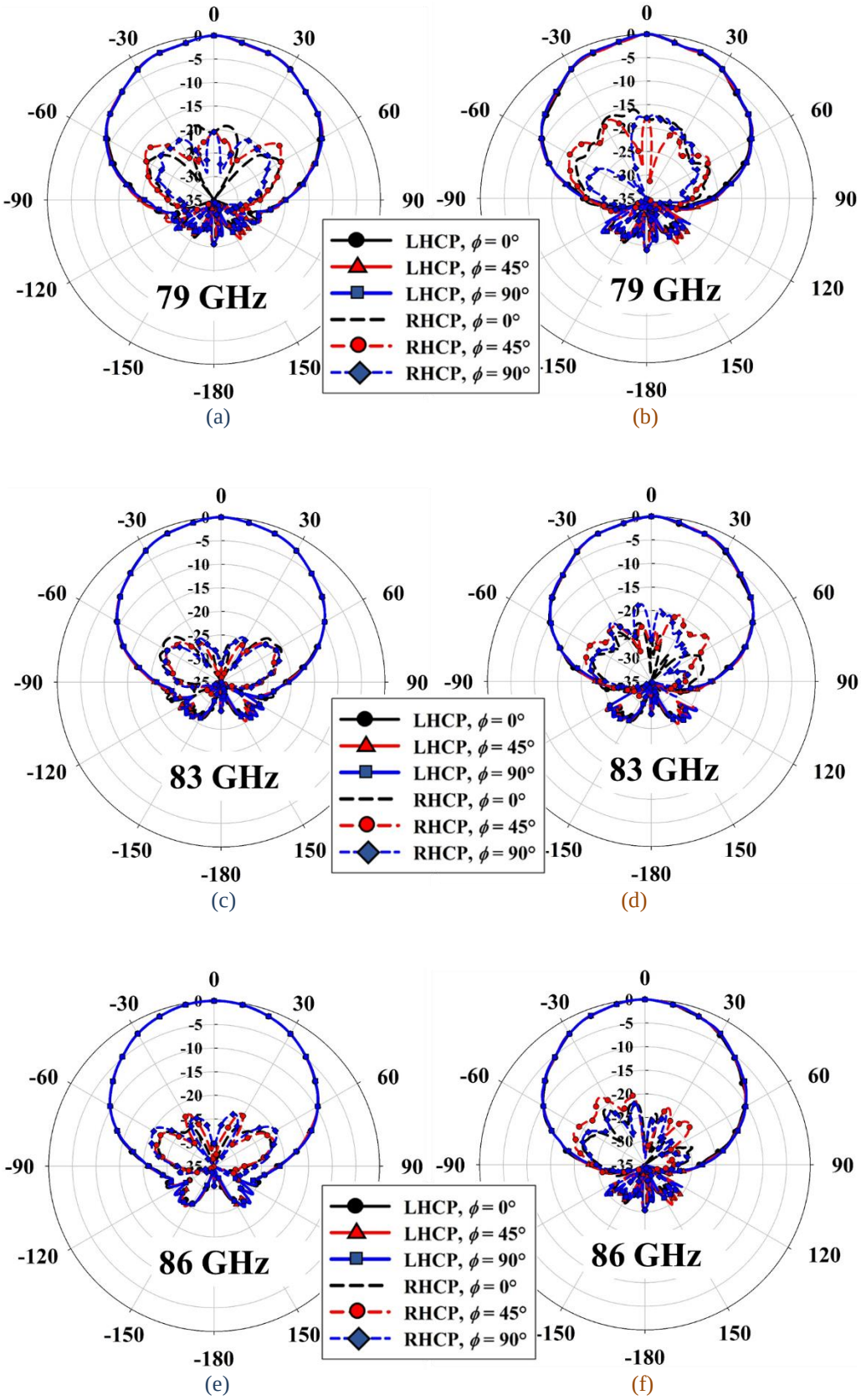

Fig. 8.5. Simulated (a,c,e) and measured (b,d,f) 2D radiation pattern of the proposed feed horn antenna.

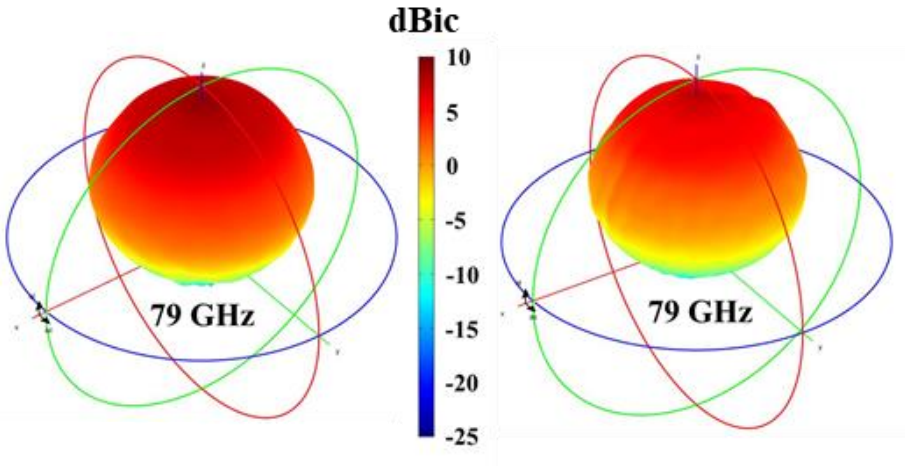

(a) (b)

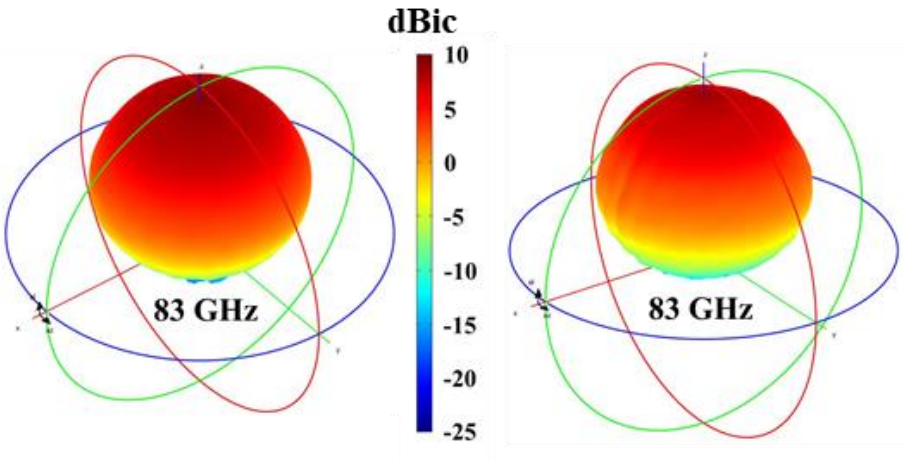

(c) (d)

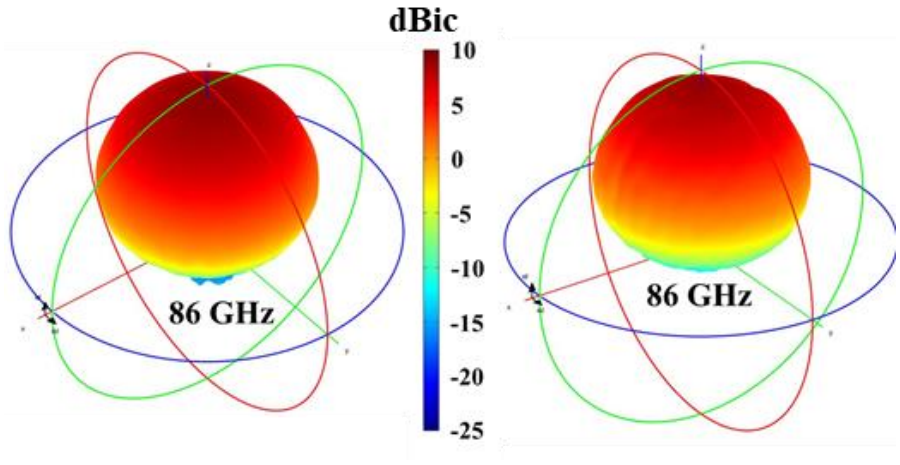

(e) (f)

Fig. 8.6. Simulated (a,c,e) and measured (b,d,f) 3D realized gain radiation pattern of the final optimized feed horn antenna.

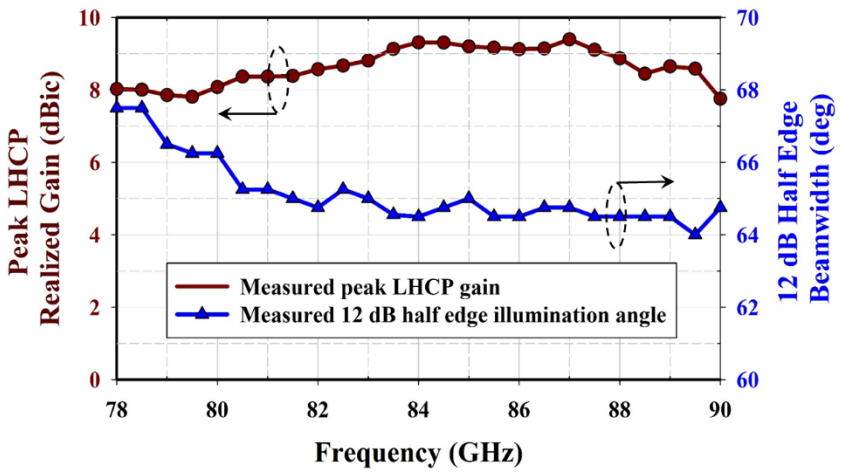

Fig. 8.7. Measured peak LHCP gain and 12 dB half edge illumination beamwidth of the proposed feed horn antenna.

The proposed feed horn antenna shows the average measured 12 dB half edge illumination of 65° over the desired matching bandwidth and meets the requirement to illuminate an offset parabolic reflector of *f/D* ratio 0.25. The feed radiation patterns are generated from HFSS simulation and incorporated as tabulated feed pattern (. cut files) into TICRA Grasp. The radiation from the feed horn and from the induced currents on the offset parabolic reflector are summed to obtain the total field. Fig. 8.8(a, b, c) shows the stable surface current distribution on the reflector with edge taper of -12 dB at 79 GHz, 83 GHz, and 86 GHz, respectively. The simulated directivity pattern of the offset reflector is presented at 79 GHz, 83 GHz, and 86 GHz, in Fig. 8.9(a, b, c). The peak simulated RHCP directivity is 35.7 dBic, 36.2 dBic, and 36.6 dBic with peak cross-polarization separation of 20 dB, 28.9 dB, and 23.3 dB at 79 GHz, 83 GHz, and 86 GHz, respectively.

The spillover is calculated using Ticra GRASP where the following equations are used to calculate the spillover loss for the reflector. When the induced PO currents are computed on a scatterer surface, the power contained in the incident field is computed by integrating the Poynting vector $\vec{P}$ over the surface. The total power *W* on the surface becomes

$$\vec{P} = \frac{1}{2}\mathrm{Re}(\vec{E} \times \vec{H}^{*})$$

$$W = -\iint_{s} \vec{P}(\vec{r}^{\,'}).n(\vec{r}^{\,'})ds^{'}$$

The spillover in dB is defined as

$$spillover = 10\log_{10}\frac{4\pi}{W}$$

where the factor 4π originates from the normalization of the feed to the power 4π watt.
The simulated spillover loss of the reflector analyzed from Ticra GRASP is 0.83 dB, which is reasonable for low *f/D* of 0.25.

The average 3 dB beamwidth is 2.5° in both φ = 0° and φ = 90° plane. The high cross-polarization level is due to the small *f/D* of the offset reflector. The cross-polarization separation can be

improved by increasing the *f*/*D* of the reflector and with narrower half edge illumination beamwidth feed sources. However, the current application of CubeSat limits the *f*/*D* to 0.25.

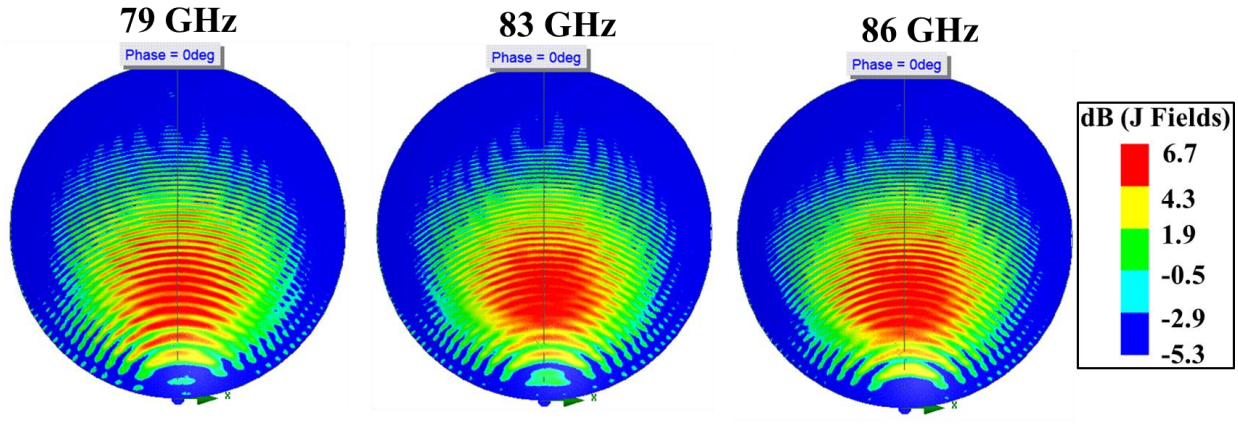

(a) (b) (c)

Fig. 8.8. Current distribution on the offset parabolic reflector simulated in Ansys HFSS at (a) 79 GHz, (b) 83 GHz and (c) 86 GHz.

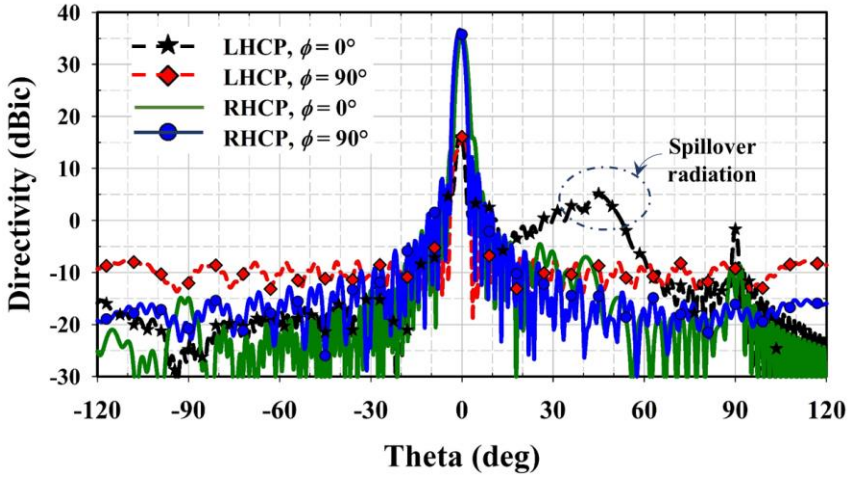

(a)

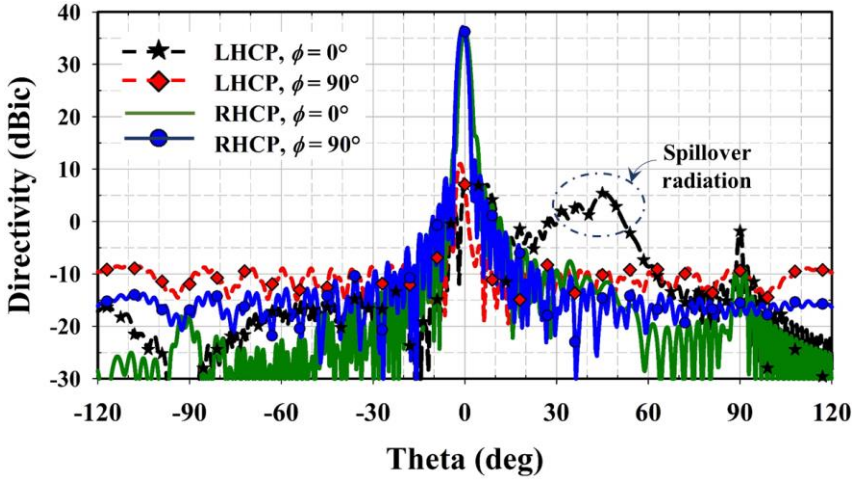

(b)

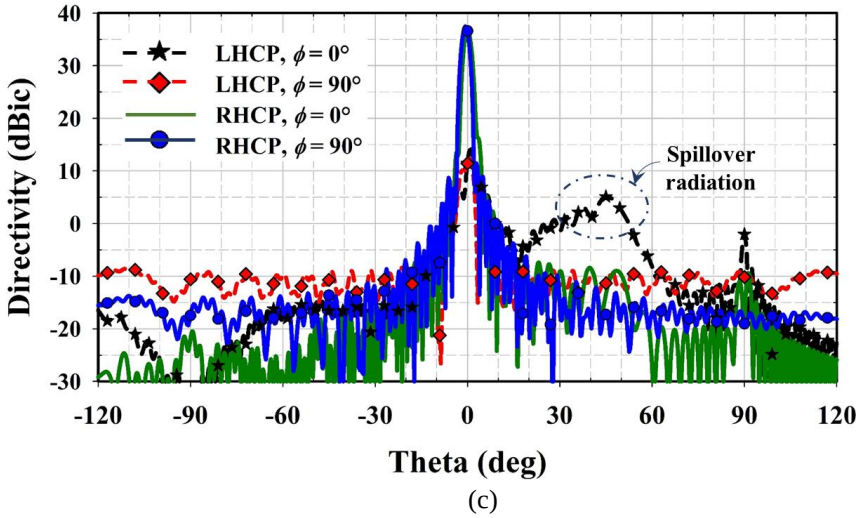

(c)

Fig. 8.9. Simulated directivity pattern of the offset parabolic reflector illuminated by the proposed feed horn at (a) 79 GHz, (b) 83 GHz and (c) 86 GHz using Ticra GRASP.

The simulated peak directivity and peak cross-polarization separation from Ticra GRASP are also compared with the Ansys HFSS-IE solver as presented in Fig. 8.10. The HFSS-IE solver uses the method of moments (MoM) technique to solve for the sources or currents on the surfaces of conducting object in open regions with linked sources.

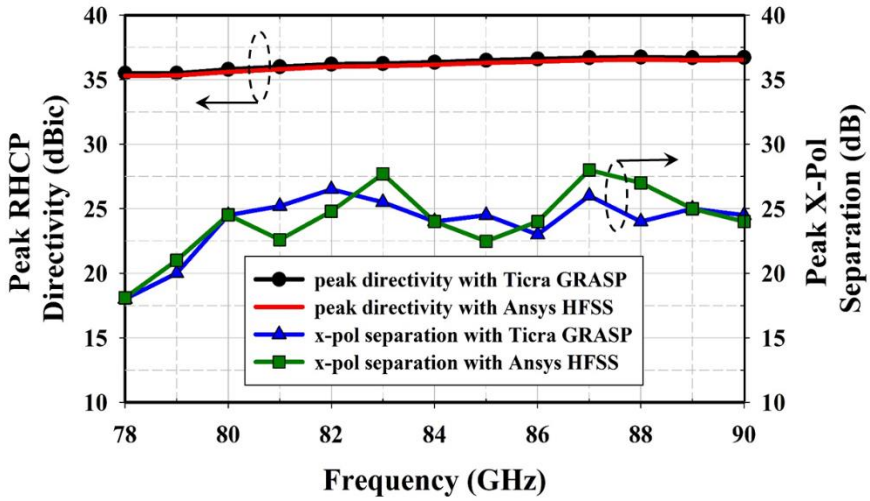

Fig. 8.10. Peak simulated RHCP directivity and peak cross-polarization separation of the offset parabolic reflector illuminated by the proposed feed horn as a function of frequency using Ticra GRASP and Ansys HFSS-IE.

Fig. 8.11 illustrates the measurement setup for the integrated feed horn and offset reflector antenna at the MVG spherical near-field facility. Fig. 8.12(a, b, c) show the measured 2D realized gain reflector pattern at 79 GHz, 83 GHz, and 86 GHz respectively. The small *f/D* of 0.25 along with the offset configuration of the reflector resulted in a high cross-polarization as seen in Fig. 8.12. The measured peak RHCP gain of the proposed feed reflector antenna is 32.92 dBic, 33.77 dBic, and 34.36 dBic at 79 GHz, 83 GHz, and 86 GHz, respectively, as presented in the 3D RHCP realized gain radiation pattern Fig. 8.13.

The beam squint phenomenon is inherent to an offset parabolic reflector when illuminated by circularly polarized primary feeds [39]. The beam squint occurs in the φ = 90° plane direction that is orthogonal to the principal offset axis of the reflector. The peak of the RHCP radiation pattern occurs at a value θ_s, for which

$$\theta_s = -\sin^{-1}\left(\frac{\lambda \sin\psi_f}{4\pi F}\right) \tag{8.1}$$

where ψ_f is the angle made by the feed at the center of the offset reflector.

At the center frequency of 83 GHz, this corresponds to the squint of -0.66° in φ = 90° plane. The measured squint angle at 83 GHz is at -0.71°, which is in a reasonable agreement to the computed value.

Fig. 8.11. The measurement setup for the fabricated prototype of the feed reflector antenna at MVG spherical near-field chamber.

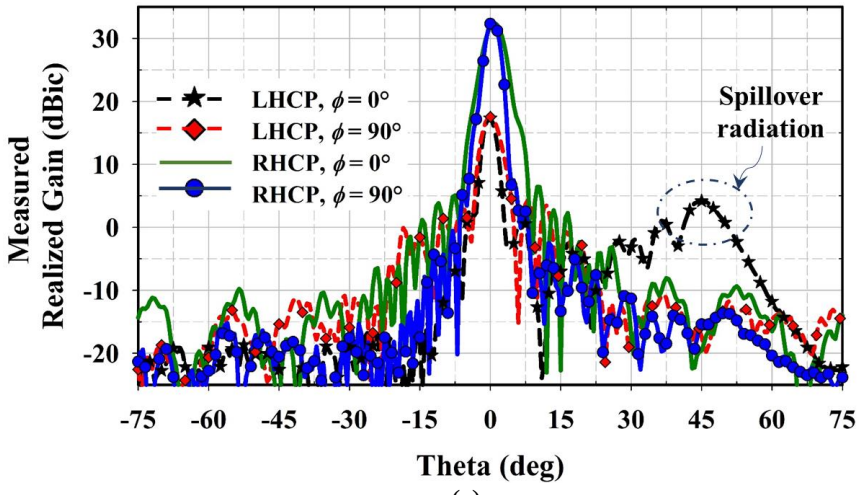

(a)

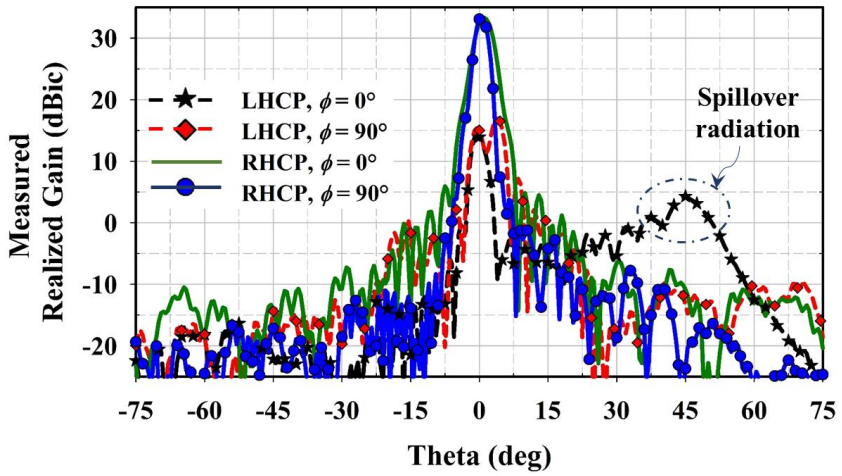

(b)

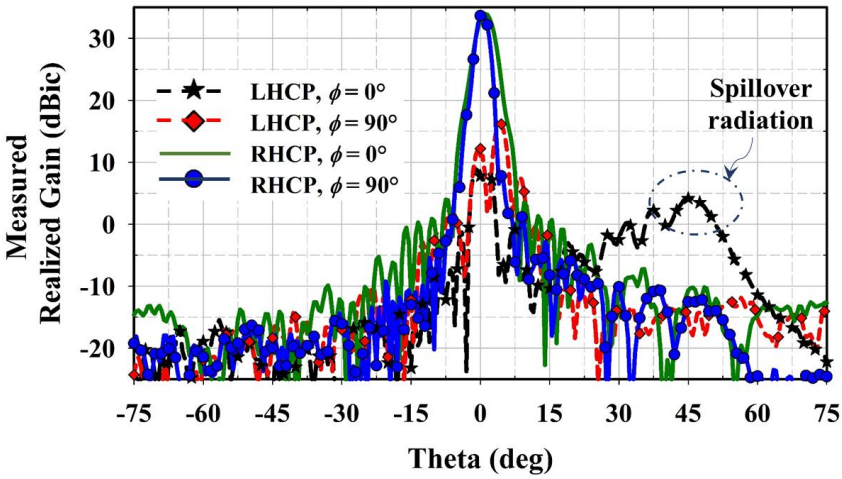

(c)

Fig. 8.12. Measured realized gain pattern of the offset parabolic reflector at (a) 79 GHz, (b) 83 GHz and (c) 86 GHz.

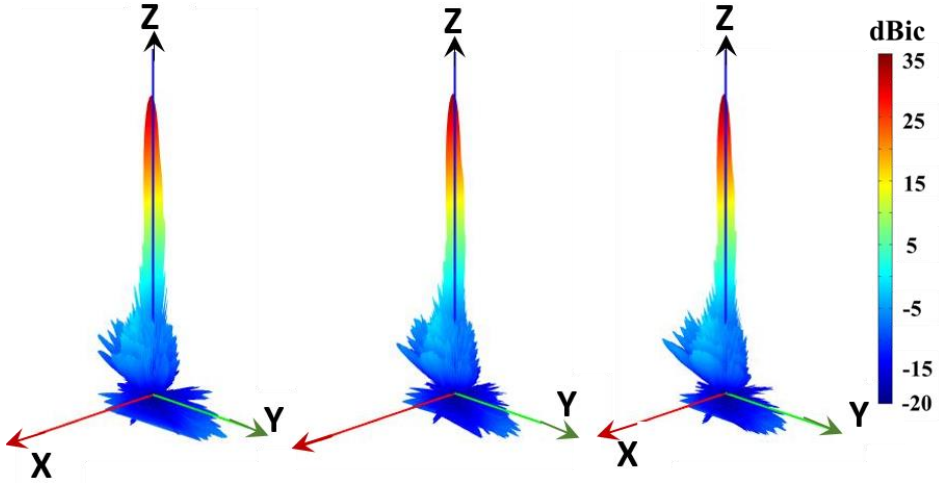

(a) (b) (c)

Fig. 8.13. Measured 3D RHCP realized gain radiation pattern of the offset parabolic reflector at (a) 79 GHz, (b) 83 GHz and (c) 86 GHz.

The average measured 3 dB beamwidth is 3° and 2.8° in φ = 0° and φ = 90° plane, respectively. Fig. 8.14 presents the peak RHCP gain and total antenna efficiency of the measured feed reflector antenna as a function of frequency. The average measured total antenna efficiency of the offset parabolic reflector is above 60% within the desired matching bandwidth from 79 GHz to 88 GHz. The total antenna efficiency includes the effect of feed horn mismatch loss, feed horn radiation efficiency, spillover and aperture efficiency of the offset reflector.

Discussion in the report is limited to the feed horn and reflector antenna design for CubeSat application with f/D = 0.25. The stringent requirement on the reflector parameter led to relatively high cross-polarization level. Applications, where space is not a constraint, a larger f/D more than 0.6 along with narrower illumination beamwidth of the feed horn, can be utilized for improved cross-polarization performance. In addition, aperture tapering and corrugations in the proposed feed aperture can be implemented to enhance the gain of the feed horn. Gimbals can be used for mechanical beam steering and beam tracking in the proposed feed reflector antenna configuration.

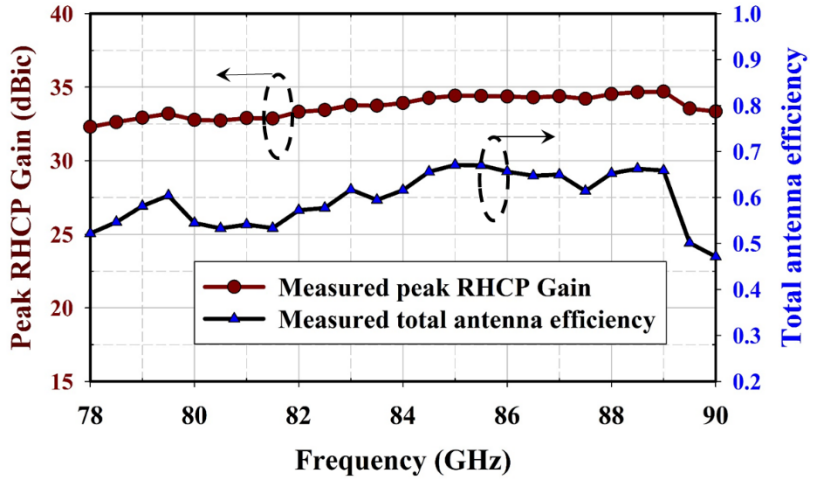

Fig. 8.14. Measured peak RHCP realized gain and total antenna efficiency of the offset parabolic reflector as a function of frequency.

9 Effect of 6U-Cubesat Chassis

The proposed feed reflector assembly is designed to be used in a CubeSat application at W-band. The impact of the CubeSat chassis on the antenna radiation performance could not be analyzed using available Ticra GRASP and thus is analyzed using shooting and bouncing rays (SBR) with simultaneously consistent implementations of PTD and Creeping wave (SBR+) features of Ansys Savant.

The position of the feed reflector assembly inside the CubeSat chassis is chosen to study the worst case antenna performance. The CAD rendering of the integrated feed reflector inside a 1U block of the 6U-CubeSat chassis and the simulated 3D RHCP gain pattern for the combined assembly are shown in Fig. 9.1(a). The comparison of 2D RHCP gain pattern of the feed reflector assembly with and without the CubeSat chassis is shown in Fig. 9.1(b). The peak simulated gain of the integrated feed reflector inside the chassis is 35.03 dBic, and the peak simulated gain of the feed reflector antenna without the CubeSat chassis is 36.1 dBic, and the cross polarization separation is 25 dB at 86 GHz. In the presence of CubeSat chassis, the sidelobe level has increased with

higher ripples, whereas the main lobe is preserved. The total simulated antenna efficiency of 61.65% is achieved for the antenna integrated inside the CubeSat chassis.

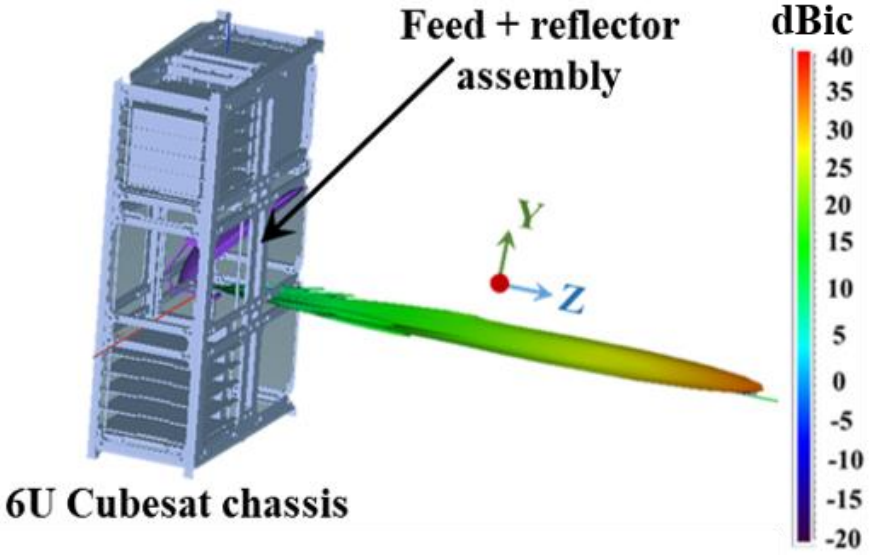

(a)

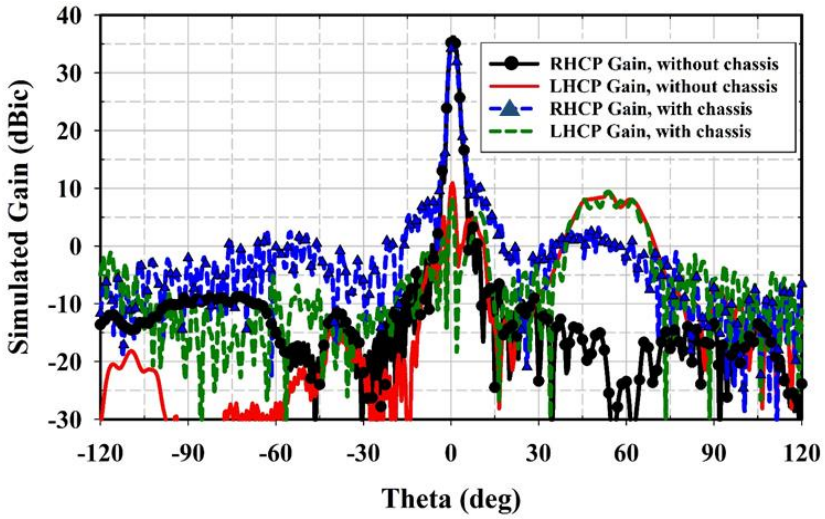

(b)

Fig. 9.1 (a) 3D of the offset parabolic reflector integrated with the proposed feed horn antenna inside 6U CubeSat chassis and (b) 2D gain pattern of the feed reflector with and without chassis, analyzed using Ansys Savant (SBR+) at 86 GHz.

10 Conclusion

A novel circular polarized feed horn is developed at W-band frequency from 79 GHz to 88 GHz that eliminates the need for an external OMT or a complex septum to generate CP waves. The detailed parametric analysis is used to determine the optimum dimension of the proposed feed horn antenna. The results of the analysis and the simulation are validated in the fabrication and measurement of the proposed feed horn antenna. The proposed feed horn is shown to have an impedance matching (S_{11} below -15 dB) and AR (below 1.2 dB) from 79.5 GHz to 88 GHz. The pattern symmetry and the stable radiation performance is also verified in the radiation pattern

measurement of the proposed feed horn antenna. The offset reflector provided peak measured RHCP realized gain of 34.36 dBic at 86 GHz. The effect of CubeSat chassis on the radiation performance of the proposed feed horn integrated with the offset parabolic reflector assembly is also simulated.

11 Future Research Work

11.1 W-band circular polarized series fed phased array antenna

The design of high gain phased array antenna as an alternative solution for high data rate W-band CubeSat application will be analyzed and developed. A high gain W-band right hand circular polarization (RHCP) series fed phased array antenna capable of single plane beam steering in the scanning range of +/- 35° with large cross polarization separation is to be designed.

A novel series fed circular polarized radiating element known as Butterfly antenna is designed and the array antenna is fabricated. The photograph of the fabricated beamforming board and aperture array is shown in Fig. 11.1.1. The integrated board is yet to be populated with 4-bit phase shifters and LNA. After the assembly, the experimental verification will be performed in the Mini compact anechoic chamber of the Antenna and Microwave Lab at San Diego State University as shown in Fig. 11.1.2

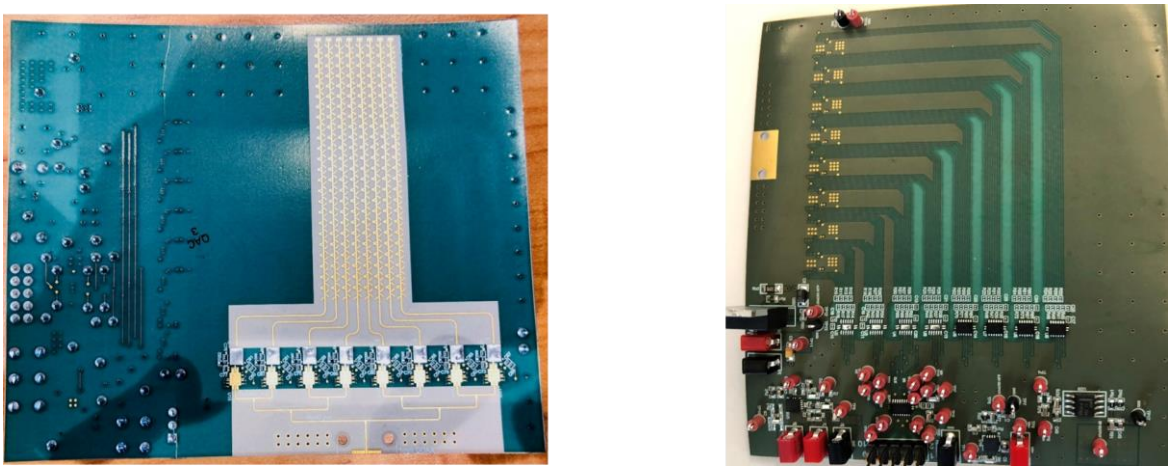

(a) (b)

Fig. 11.1.1 Photograph of the proposed fabricated integrated beamforming phased array antenna (a) top view (b) bottom view.

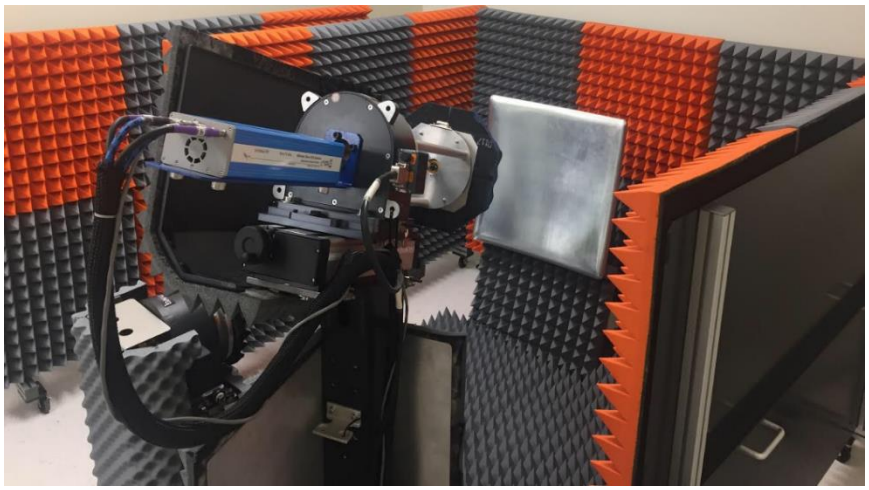

Fig. 11.1.2 Mini Compact anechoic chamber at antenna and microwave lab at San Diego State University.

11.2 Ku-band parabolic cylindrical reflector phased array feed for single plane scanning

I am currently working on the design and analysis of Ku band beam scanning in a parabolic cylindrical reflector using phased array as a feed source. The parabolic cylindrical reflector provides wide beam scanning at low *f*/*D* compared to a conventional parabolic reflector antenna. Fig. 11.2.1 shows the illustration of the proposed concept presenting linear source feed of phased array arranged along the focal line of the cylindrical axis of the reflector.

The phased array feed source will be scanned using the integrated beamforming board which will also be developed along with the array aperture. Based on the beam scanning of the feed, the resultant secondary pattern of the reflector will be investigated and analysed. In addition, the sidelobe level will also be controlled along with the beam steering by distinct control on the excitation weights.

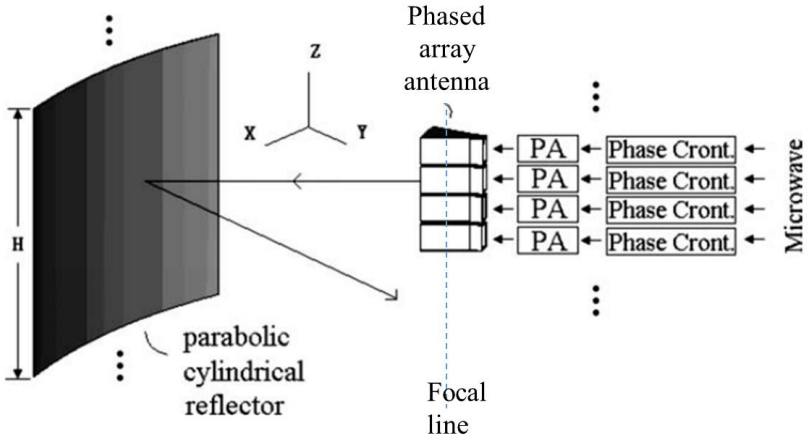

Fig. 11.2.1 Illustration of the proposed wide scanning parabolic cylindrical reflector antenna using phased array feed source at Ku-band.

12 Acknowledgment

I would like to thank MVG for the measurement of the feed horn and reflector antenna at their spherical near-field measurement facility. This work is supported by the Office of Naval Research (ONR) grant # N00014-16-1-2166.

13 References

[1] L. Shafai, S. K. Sharma and S. Rao, “Handbook of Reflector Antennas and Feed Systems, Volume II: Feed Systems”, *Artech House*, USA, June 2013.

[2] S. K. Sharma, L. Shafai and S. Rao, “Handbook of Reflector Antennas and Feed Systems, Volume I: Theory and Design of Reflectors”, *Artech House*, USA, June 2013.

[3] S. K. Sharma, L. Shafai, and M. Barakat, “Ka-band Dual Circularly Polarized Feed Horn for Reflector Antenna for Satellite Communications”, *International Symposium on Antenna Technology and Applied Electromagnetics*, Saint-Malo, France, June 15-17, 2005, pp. 82-83.

[4] S. Bhardwaj and J. L. Volakis, "Hexagonal Waveguide Based Circularly Polarized Horn Antennas for Sub-mm-Wave/Terahertz Band," in *IEEE Transactions on Antennas and Propagation*, vol. 66, no. 7, pp. 3366-3374, July 2018.

[5] A. M. Boifot, E. Lier and T. Schaug-Pettersen, "Simple and broadband orthomode transducer (antenna feed)," in *IEE Proceedings H - Microwaves, Antennas and Propagation*, vol. 137, no. 6, pp. 396-400, Dec 1990.

[6] J. A. Ruiz-Cruz, J. R. Montejo-Garai, C. A. Leal-Sevillano and J. M. Rebollar, "Orthomode Transducers With Folded Double-Symmetry Junctions for Broadband and Compact Antenna Feeds," in *IEEE Transactions on Antennas and Propagation*, vol. 66, no. 3, pp. 1160-1168, March 2018.

[7] J. A. Ruiz-Cruz, J. R. Montejo-Garai, J. M. Rebollar and J. M. Montero, "C-band orthomode transducer for compact and broadband antenna feeders," in *Electronics Letters*, vol. 45, no. 16, pp. 813-814, July 30 2009.

[8] M. Esquius-Morote, M. Mattes and J. R. Mosig, "Orthomode Transducer and Dual-Polarized Horn Antenna in Substrate Integrated Technology," in *IEEE Transactions on Antennas and Propagation*, vol. 62, no. 10, pp. 4935-4944, Oct. 2014.

[9] R. Garcia, F. Mayol, J. M. Montero and A. Culebras, "Circular polarization feed with dual-frequency OMT-based turnstile junction," in *IEEE Antennas and Propagation Magazine*, vol. 53, no. 1, pp. 226-236, Feb. 2011.

[10] A. A. Sakr, W. Dyab and K. Wu, "Design Methodologies of Compact Orthomode Transducers Based on Mechanism of Polarization Selectivity," in *IEEE Transactions on Microwave Theory and Techniques*, vol. 66, no. 3, pp. 1279-1290, March 2018.

[11] G. M. Coutts, "Wideband Diagonal Quadruple-Ridge Orthomode Transducer for Circular Polarization Detection," in *IEEE Transactions on Antennas and Propagation*, vol. 59, no. 6, pp. 1902-1909, June 2011.

[12] G. Virone, O. A. Peverini, M. Lumia, M. Z. Farooqui, G. Addamo and R. Tascone, "W-Band Orthomode Transducer for Dense Focal-Plane Clusters," in *IEEE Microwave and Wireless Components Letters*, vol. 25, no. 2, pp. 85-87, Feb. 2015.

[13] G. M. Coutts, "Octave Bandwidth Orthomode Transducers for the Expanded Very Large Array," in *IEEE Transactions on Antennas and Propagation*, vol. 59, no. 6, pp. 1910-1917, June 2011.

[14] W. Hongjian, Y. Min, L. Guang and C. Xue, "Potter Horn and Compact Orthomode Transducer at 150 GHz," in *IEEE Transactions on Antennas and Propagation*, vol. 62, no. 10, pp. 5403-5405, Oct. 2014.

[15] M. J. Franco, "A High-Performance Dual-Mode Feed Horn for Parabolic Reflectors with a Stepped-Septum Polarizer in a Circular Waveguide [Antenna Designer's Notebook]," in *IEEE Antennas and Propagation Magazine*, vol. 53, no. 3, pp. 142-146, June 2011.

[16] C. A. Leal-Sevillano, K. B. Cooper, J. A. Ruiz-Cruz, J. R. Montejo-Garai and J. M. Rebollar, "A 225 GHz Circular Polarization Waveguide Duplexer Based on a Septum Orthomode Transducer Polarizer," in *IEEE Transactions on Terahertz Science and Technology*, vol. 3, no. 5, pp. 574-583, Sept. 2013.

[17] N. C. Albertsen and P. Skov-Madsen, "A Compact Septum Polarizer," in *IEEE Transactions on Microwave Theory and Techniques*, vol. 31, no. 8, pp. 654-660, Aug. 1983.

[18] I. Kim, J. M. Kovitz and Y. Rahmat-Samii, "Enhancing the Power Capabilities of the Stepped Septum Using an Optimized Smooth Sigmoid Profile," in *IEEE Antennas and Propagation Magazine*, vol. 56, no. 5, pp. 16-42, Oct. 2014.

[19] Ming hui chen, "*Waveguide polarizer and antenna assembly*" US Patent # 6118412 granted Sep. 12, 2000.

[20] J. Bornemann and V. A. Labay, "Ridge waveguide polarizer with finite and stepped-thickness septum," in *IEEE Transactions on Microwave Theory and Techniques*, vol. 43, no. 8, pp. 1782-1787, Aug 1995.

[21] R. Nair, A. Kamal and S. Gupta, "A high gain dielectric loaded biconical horn for circular polarization," in *IEEE Transactions on Antennas and Propagation*, vol. 27, no. 6, pp. 860-861, November 1979.

[22] Shih-Wei Wang, Chih-Hung Chien, Chun-Long Wang and Ruey-Beei Wu, "A circular polarizer designed with a dielectric septum loading," in *IEEE Transactions on Microwave Theory and Techniques*, vol. 52, no. 7, pp. 1719-1723, July 2004.

[23] H. Jin, Y. M. Huang, H. Jin and K. Wu, "E-band Substrate Integrated Waveguide Orthomode Transducer Integrated with Dual-Polarized Horn Antenna," in *IEEE Transactions on Antennas and Propagation*, vol. PP, no. 99, pp. 1-1.

[24] M. Narasimhan and M. Sheshadri, "Propagation and radiation characteristics of dielectric loaded corrugated dual-frequency circular waveguide horn feeds," in *IEEE Transactions on Antennas and Propagation*, vol. 27, no. 6, pp. 858-860, November 1979.

[25] G. G. Gentili, P. Bolli, R. Nesti, G. Pelosi and L. Toso, "High-Order FEM Mode Matching Analysis of Circular Horns With Rotationally Symmetric Dielectrics," in *IEEE Transactions on Antennas and Propagation*, vol. 55, no. 10, pp. 2915-2918, Oct. 2007.

[26] A. G. Martin, "Radiation from dielectric sphere loaded horns," in *Electronics Letters*, vol. 14, no. 1, pp. 17-18, January 5 1978.

[27] R. Nevels, "An analysis of a two-dimensional dielectric covered corrugated antenna feed horn," in *IEEE Transactions on Antennas and Propagation*, vol. 32, no. 8, pp. 877-880, August 1984.

[28] J. Chatterjee and W. Croswell, "Waveguide excited dielectric spheres as feeds," in *IEEE Transactions on Antennas and Propagation*, vol. 20, no. 2, pp. 206-208, Mar 1972.

[29] N. Chahat, R. E. Hodges, J. Sauder, M. Thomson, E. Peral and Y. Rahmat-Samii, "CubeSat Deployable Ka-Band Mesh Reflector Antenna Development for Earth Science Missions," in *IEEE Transactions on Antennas and Propagation*, vol. 64, no. 6, pp. 2083-2093, June 2016.

[30] N. Chahat, R. E. Hodges, J. Sauder, M. Thomson and Y. Rahmat-Samii, "The Deep-Space Network Telecommunication CubeSat Antenna: Using the deployable Ka-band mesh reflector antenna.," in *IEEE Antennas and Propagation Magazine*, vol. 59, no. 2, pp. 31-38, April 2017.

[31] N. E. Chahat, "A mighty antenna from a tiny CubeSat grows," in *IEEE Spectrum*, vol. 55, no. 2, pp. 32-37, February 2018.

[32] S. Gao, Y. Rahmat-Samii, R. E. Hodges and X. X. Yang, "Advanced Antennas for Small Satellites," in *Proceedings of the IEEE*, vol. 106, no. 3, pp. 391-403, March 2018.

[33] R. E. Hodges, N. Chahat, D. J. Hoppe and J. D. Vacchione, "A Deployable High-Gain Antenna Bound for Mars: Developing a new folded-panel reflectarray for the first CubeSat mission to Mars.," in *IEEE Antennas and Propagation Magazine*, vol. 59, no. 2, pp. 39-49, April 2017.

[34] I. A. Osaretin, M. W. Shields, J. A. M. Lorenzo and W. J. Blackwell, "A Compact 118-GHz Radiometer Antenna for the Micro-Sized Microwave Atmospheric Satellite," in *IEEE Antennas and Wireless Propagation Letters*, vol. 13, pp. 1533-1536, 2014.

[35] G. Mishra, A. T. Castro, S. K. Sharma and J. S. Chieh, "W-band feed horn with polarizer structure for an offset reflector antenna for cubesat applications," 2017 *IEEE International Symposium on Antennas and Propagation & USNC/URSI National Radio Science Meeting*, San Diego, CA, 2017, pp. 557-558.

[36] Thomas A. Milligan, "Reflector Antennas," in *Modern Antenna Design*, 1, Wiley-IEEE Press, 2005, pp.580.

[37] Xu, C., Tantawi, S. and Wang, J. (2014) Novel X Band Compact Waveguide Dual Circular Polarizer. Cornell University Library, 1406.7266.

[38] Custom Microwave Inc. http://custommicrowave.com/

[39] N. A. Adatia and A. W. Rudge, "Beam squint in circularly polarised offset-reflector antennas," in *Electronics Letters*, vol. 11, no. 21, pp. 513-515, 16 October 1975.

14 Appendix

Geometric Optics Analysis in Matlab

This example deals with analyzing offset fed parabolic reflector antenna using Ray optics method or Aperture distribution method as discussed in section 5.2.2.

The following data was used:

Reference: R. E. Collin, "Antennas and Radio wave propagation", McGraw-Hill Higher Education, Feb 1, 1985.

- Projected aperture diameter =1.2m
- Feed tilt angle = 26.6^0
- Focal length f = 48.77 cm
- Frequency =12 GHz

Circular waveguide feed pattern *TE11* mode given by

$$e(\theta_0) = (1 + 0.81\cos\theta_0)\frac{J_1(\pi \sin\theta_0)}{\sin\theta_0}$$

The focal-plane aperture field are as follows:

$$E_{ax} = \frac{4fe^{-j2k_0 f}e(\theta_0)}{\left(4f^2+\rho^2\right)\left[4f^2+\rho^2-4fy\sin\psi+\left(4f^2-\rho^2\right)\cos\psi\right]} \times \left[2xy\left(1-\cos\psi\right)-4fx\sin\psi\right]$$

$$E_{ay} = \frac{4fe^{-j2k_0 f}e(\theta_0) \times \left[\left(4f^2+\rho^2-2x^2\right)+\left(4f^2-\rho^2+2x^2\right)\cos\psi-4fy\sin\psi\right]}{\left(4f^2+\rho^2\right)\left[4f^2+\rho^2-4fy\sin\psi+\left(4f^2-\rho^2\right)\cos\psi\right]}$$

$$E_{az} = 0$$

where, $\rho^2 = x^2 + y^2$ and $\theta_0 = \cos^{-1}\left(\frac{4f^2-\rho^2}{4f^2+\rho^2}\cos\psi - \frac{4fy}{4f^2+\rho^2}\sin\psi\right)$

A. Part 1. Aperture Field Distribution Profile

```
clc;close all;clear all;
% Defining the parameters
psi=26.6*pi/180;          % Tilt Angle
f=0.4877;                 % Focal Length
freq= 12e9;               % Operating Frequency
velocity=3e8;
k=2*pi*freq/velocity;      % Wave Number
a=0.6;                    % Radius of the projected Aperture
as=0.016;                 %Radius of the feed source
c=0.230574748;            % Center of the projected aperture
lambda=velocity/freq;
r=1000;
deg= 180/pi;

% Feed Profile
theta_0=-pi/2:0.01:pi/2;
e_theta_0= (1+ (0.81.*cos(theta_0))).*besselj(1,pi.*sin(theta_0))./(sin(theta_0));
figure;
plot(theta_0*180/pi,e_theta_0/max(e_theta_0),'linewidth',2.5);
grid on;
title('Feed Distribution Profile','fontsize',12,'fontname','cambria');
xlabel('\theta, degrees','fontsize',12,'fontname','cambria');
ylabel('Relative Field','fontsize',12,'fontname','cambria');

% Calculating the aperture field Eax and Eay
x1= linspace(-a,a,30);
y1=linspace(-c-a,-c+a,30);
 [x,y]= meshgrid(x1,y1);
rho = sqrt(x.^2 + y.^2);
theta_0= acos(((4*(f^2)- (rho.^2)).*cos(psi) - (4*f.*y.*sin(psi))./((4*(f^2)+(rho.^2))));
e_theta_0= (1+ (0.81.*cos(theta_0))).*besselj(1,pi.*sin(theta_0))./(sin(theta_0));
Den= (4*(f^2)+(rho.^2)).*((4*(f^2)+(rho.^2))-(4*f.*y.*sin(psi)) + (4*(f^2)- (rho.^2)).*cos(psi));
 Num1= 4*f*exp(-j*2*k*f).*e_theta_0;
Num2= (2.*x.*y.*(1-cos(psi)) - (4*f.*x.*sin(psi)));
Num3= ((4*(f^2)+(rho.^2)- (2.*(x.^2)))+ (4*(f^2)-(rho.^2)+ (2.*(x.^2))).*cos(psi) -
(4.*f.*y.*sin(psi)));
E_ax = Num1.*Num2./Den;                          % Ex aperture field
E_ay= (Num1).*(Num3)./(Den);                     % Ey aperture field
figure;
circles(0,-c,a,'facecolor','none','edgecolor','b','linewidth',1.5);    % Plotting the projected
aperture
axis equal;

hx=E_ax;
hy=E_ay;
     hx(x > (sqrt(a^2- (y+c).^2))) = 0;
     hx(x < (-sqrt(a^2- (y+c).^2))) = 0;
     hy(x > (sqrt(a^2- (y+c).^2))) = 0;
     hy(x < (-sqrt(a^2- (y+c).^2))) = 0;
hold on;
h2=quiver(x,y,real(hx),real(hy),'linewidth',1.3);    % Plot of the Aperture Field
```

```
 xlim([-0.65 0.65]);
 ylim([-0.85 0.45]);
 title('Aperture Field Distribution Profile','fontsize',12,'fontname','cambria');
```

B. Part 2. Gain and Efficiency ignoring the effect of feed blockage

```
 dx = 1e-3;
dy = 1e-3;
X = -a:dx:a;
Y = -c-a:dy:-c+a;
[x,y] = meshgrid(X,Y);
rho = sqrt(x.^2+y.^2);
theta_0= acos(((4*(f^2)- (rho.^2)).*cos(psi) - (4*f.*y.*sin(psi))./((4*(f^2)+(rho.^2))));
e_theta_0= (1+ (0.81.*cos(theta_0))).*besselj(1,pi.*sin(theta_0))./(sin(theta_0));
Den= (4*(f^2)+(rho.^2)).*((4*(f^2)+(rho.^2))-(4*f.*y.*sin(psi)) + (4*(f^2)- (rho.^2)).*cos(psi));
Num1= 4*f*exp(-1i*2*k*f).*e_theta_0;

Num2= (2.*x.*y.*(1-cos(psi)) - (4*f.*x.*sin(psi)));
Num3= ((4*(f^2)+(rho.^2)- (2.*(x.^2)))+ (4*(f^2)-(rho.^2)+ (2.*(x.^2))).*cos(psi) -
(4.*f.*y.*sin(psi)));
E_ax = Num1.*Num2./Den;
E_ay= (Num1).*(Num3)./(Den);

h= abs(E_ay).^2*dx*dy;
h(x > (sqrt(a^2- (y+c).^2))) = 0;
h(x < (-sqrt(a^2- (y+c).^2))) = 0;
    hy= sum(sum(h));

 fun= @(theta_0) (abs((1+
(0.81.*cos(theta_0))).*besselj(1,pi.*sin(theta_0))./(sin(theta_0))).^2.*(2*pi.*sin(theta_0)));
deng= integral(fun,0,pi);

gain= (4*pi/(lambda^2))*hy/deng;
Gain_dB= 10*log10(abs(gain));
sprintf('\b Gain of the offset feed parabolic dish without feed blockage = %.3f dB', Gain_dB)


totaleff= gain*lambda^2/(4*(pi^2)*(a^2))*100;
sprintf('\b Total Efficiency of the offset feed parabolic dish without feed blockage = %.3f %%',
totaleff)
```

```
ans =
 Gain of the offset feed parabolic dish = 42.414 dB

ans =
 Total Efficiency of the offset feed parabolic dish = 76.666 %
```

C. Part 3. H-Plane Radiation pattern and Maximum relative Cross Pol Level

```
dTheta = pi/3000;
theta0 = 0;
thetaEnd = 15*pi/180;
dx = 1e-3;
dy = 1e-3;
theta = theta0:dTheta:thetaEnd;
X = -a:dx:a;
Y = -c-a:dy:-c+a;
[x,y] = meshgrid(X,Y);
rho = sqrt(x.^2+y.^2);
theta_0= acos(((4*(f^2)- (rho.^2)).*cos(psi) - (4*f.*y.*sin(psi))./((4*(f^2)+(rho.^2))));
e_theta_0= (1+ (0.81.*cos(theta_0))).*besselj(1,pi.*sin(theta_0)./(sin(theta_0));
Den= (4*(f^2)+(rho.^2)).*((4*(f^2)+(rho.^2))-(4*f.*y.*sin(psi)) + (4*(f^2)- (rho.^2)).*cos(psi));
Num1= 4*f*exp(-1i*2*k*f).*e_theta_0;
Num2= (2.*x.*y.*(1-cos(psi)) - (4*f.*x.*sin(psi)));
Num3= ((4*(f^2)+(rho.^2)- (2.*(x.^2)))+ (4*(f^2)-(rho.^2)+ (2.*(x.^2))).*cos(psi) -
(4.*f.*y.*sin(psi)));
E_ax = Num1.*Num2./Den;
E_ay= (Num1).*(Num3)./(Den);
E_co = zeros(size(theta));
for ii = 1:length(theta)
    fy = (E_ay).*exp(1i*k.*sin(theta(ii)).*x)*dx*dy;
    fy(x > (sqrt(a^2- (y+c).^2))) = 0;
    fy(x < (-sqrt(a^2- (y+c).^2))) = 0;
    hy= sum(sum(fy));
    E_co(ii) = (1i*k*exp(-1i*k*r)/(2*pi*r)).*hy.*cos(theta(ii));
    fx = (E_ax).*exp(1i*k.*sin(theta(ii)).*x)*dx*dy;
    fx(x > (sqrt(a^2- (y+c).^2))) = 0;
    fx(x < (-sqrt(a^2- (y+c).^2))) = 0;
    hx= sum(sum(fx));
    E_cross(ii) = (1i*k*exp(-1i*k*r)/(2*pi*r)).*hx;
end
maximumy = max(20*log10(abs(E_co)));
figure;
ax = axes;
hold(ax,'on');
plot(deg*(theta0: dTheta: thetaEnd), 20*log10(abs(E_co))-maximumy,'linewidth',2.5);
grid on;
plot(deg*(theta0: dTheta: thetaEnd), 20*log10(abs(E_cross))-maximumy,'r','linewidth',2.5);
legend('co-polarized','cross-polarized');
ylabel('Relative Power, dB','fontsize',12,'fontname','cambria');
xlabel('\theta, degrees','fontsize',12,'fontname','cambria');
[maxx,indexx]= max(20*log10(abs(E_cross))-maximumy);
sprintf('\b The maximum relative cross pol level is= %.3f dB occuring at an angle of %.1f deg',
maxx,theta(indexx)*180/pi)
```

```
ans =
 The maximum relative cross pol level is= -22.127 dB occuring at an angle of
1.0 deg
```